Chemical Engineering Science 317 (2025) 122129

Contents lists available at ScienceDirect

Chemical Engineering Science

journal homepage: www.elsevier.com/locate/ces

Particle-resolved lattice Boltzmann simulations for sedimentation of catalyst particles involving coke deposition

Yiqi Song [a,b], Xue Li [a,*], Mao Ye [a,*], Zhongmin Liu [a,b]

[a] National Engineering Research Center of Lower-Carbon Catalysis Technology, Dalian Institute of Chemical Physics, Chinese Academy of Sciences, Dalian 116023, China
[b] University of Chinese Academy of Sciences, Beijing 100049, China

ARTICLE INFO

Keywords:
Catalyst particle
Coke deposition
Particulate two-phase flow
Immersed Boundary-lattice Boltzmann method

ABSTRACT

Catalyst deactivation by coke deposition in heterogeneous catalysis critically impacts reaction kinetics, yet its effects on particulate flows remain poorly understood. This work employs a particle-resolved immersed boundary-lattice Boltzmann method to analyze coke-influenced particle motion and particle–fluid interaction during sedimentation. The results reveal that for single/multiple particles, coke deposition on the catalyst particles gradually increases the particle density and accelerates the settling velocity of particles. When the reaction rate increases to certain extent, there exists a critical particle Reynolds number beyond which the vortex shedding around the catalyst appears, leading to a significant change in the flow pattern and particles motion. For settling of multiple particles, the initial release positions affect the movement of particles. Moreover, by analyzing the change of coke deposition rate during sedimentation, it is proved that the deactivation of catalyst is heterogeneous, which is caused by the uneven concentration distribution.

1. Introduction

Particulate two-phase flows are commonly encountered in natural and industrial processes. Especially in industrial catalytic processes (Tian et al., 2015; Wang et al., 2022a), particles are used as catalyst for either promoting the reaction rate or altering the reaction paths to enhance the on-target production of important chemicals. Though particulate two-phase flows in these heterogeneous catalytic reactors have been the topic of intensive research for many decades, it remains a non-trivial task to understand the fluid-particle interaction at the individual particle scale.

Numerous researches have been reported to understand complex interactions, chemical reactions, and hydrodynamic behavior of particles in two-phase flow by means of experimental (Eloul et al., 2020; Liu et al., 2020) and numerical simulation methods (Arcidiacono et al., 2008; Li et al., 2013; Lu et al., 2018). For instance, Liu et al. (Liu et al., 2020) experimentally investigated the effect of chemical reactions on particle fluctuating motions, and found that the nonuniform release of gaseous products directly accounts for particle motion. Luo et al. (Luo et al., 2018) utilized immersed boundary method (IBM) to investigate the combustion of char particle and found that the chemical reactions increase the drag force of a reactive particle compared to an inert particle. Zhao and Xu (Zhao and Xu, 2022) used immersed boundary lattice Boltzmann method (IB-LBM) to analyze the effect of the reaction on the horizontal motion of the particles by simulating the settling of two particles in parallel in a corrosive liquid. These results indicate that the particle–fluid interaction is strongly affected by the chemical reactions near the particle surface. Ou et al. (Ou et al., 2022) studied the shrinking reactive particle and further revealed detailed interphase heat/mass transfer near the reaction particles. Basically, the chemical reactions first affect particle–fluid interactions, lead to strongly irregular hydrodynamic behavior, and consequently vary mass transfer process in both space and time. The aforementioned studies, however, focus mainly on the non-catalytic reactions.

For heterogeneous catalytic reactions in which particles are used as catalyst, basically the reaction would change not only the physical properties but also the catalytic activity of catalyst particles. In industrially important methanol-olefins (MTO) (Lin et al., 2022) and fluid catalytic cracking (FCC) (Vogt and Weckhuysen, 2015) processes, for example, coke deposition over the zeolite catalyst is unavoidable (Yang et al., 2021a; Zhou et al., 2021). It has been shown that the formation of coke could result in the blockage of nanopores in zeolites, enabling the change of micro-structure characteristics and reduction of reaction activity of the catalyst (Behnam et al., 2010; Wehinger et al., 2015). In

* Corresponding authors.
E-mail addresses: lixue@dicp.ac.cn (X. Li), maoye@dicp.ac.cn (M. Ye).

https://doi.org/10.1016/j.ces.2025.122129
Received 20 March 2025; Received in revised form 23 June 2025; Accepted 28 June 2025
Available online 29 June 2025

particular, Yang et al. (Yang et al., 2021b) applied the particle scale model coupled with the reaction kinetics to learn the coke deposition and the consequent effects on the physical property and activity of catalyst in methane cracking reaction. Wang et al. (Wang et al., 2022b) investigated the coke deposition at the pore-scale, and evaluated the interplay between coke deposition and mass transfer. It should be stressed that, while above studies are concerning about the impact of chemical reaction on catalyst structure property and reaction activity, less effort has so far been contributed to the hydrodynamic behavior of catalyst particles experiencing continuous coke deposition during reaction. Actually, coke deposition is an important dynamic process closely coupled to reaction and fluid flow in industrial reactors. As pointed out by Gottifredi and Froment (Gottifredi and Froment, 1997), coke content changes the concentration and rate profiles of fluid, resulting in a transient behavior. The coke deposition is closely related to the reaction rate, which could induce the fluctuation of distribution of species in fluid flow around catalyst and alter the particle–fluid interaction and thus the motion of particles.

There are many different direct numerical simulation (DNS) methods that can be used for simulating two-phase flows. These DNS methods include but not limit to the volume of fluid (VOF), smoothed particle hydrodynamics (SPH), finite volume method (FVM) and LBM. Considering the advantages in high efficiency in computation, code development, fluid–solid boundary treatment, as well as the scalability for reacting particulate two-phase flows, we use the IB-LBM framework to investigate the effect of coke deposition on particle hydrodynamic behavior and particle–fluid interaction at individual particle scale. In doing so, we consider the sedimentation of individual catalyst in heterogeneous reaction processes. In fact, the hydrodynamic behavior of individual particles during settling under gravity have been intensively studied. For instance, a classical phenomenon frequently observed is that, if two particles in series are freely released in a channel, they would experience the drafting, kissing and tumbling (DKT) process. Several studies are shown that the hydrodynamic interaction between settling particles could be influenced by a wide variety of factors such as particles size (Shao et al., 2005; Wang et al., 2014), density (Ghosh and Kumar, 2020; Nie et al., 2017; Nie and Lin, 2020), initial position (Liu et al., 2021; Pu et al., 2023), thermal convection (Yu et al., 2006; Yang et al., 2016; Gan et al., 2003), reaction rates (Maier et al., 2021), and turbulent fluctuation (Sajjadi et al., 2018, 2017, 2016). So far, the hydrodynamic behaviors of catalyst particles undergoing continuous coke deposition, particle density increase, and reaction rate reduction during sedimentation are still incomplete. In this work, therefore, the consequences induced by coke deposition on catalyst, which is a dynamic process closely coupled to the reaction and fluid flow, are concerned.

For the reactive flows (with either endothermic or exothermic reactions) in catalytic processes, some chemical and physical properties of both fluid and catalyst particles would change with temperature, eventually affecting the particle motion and reaction rate. For example, Zhang et al. showed the effects of thermal effect on particle hydrodynamic behavior and particle–fluid interaction under medium and low Grashof number (Zhang et al., 2024, 2023). However, this paper aims at understanding the influence of coke deposition on the particle–fluid interaction via changing particle properties (density), and does not incorporate the effect of thermal gradient caused by the catalytic reaction. A comprehensive DNS model taking heat transfer, porous structure, coke formation, and catalytic reaction into account for studying hydrodynamic behavior of single catalyst particle is still under development.

The remainder of this paper is organized as follows: the research objective and numerical methods are introduced in Secs. II and III. Then in Sec. IV, the fluid–particle interaction and the particle motion for the settling of an individual particle, two particles in parallel, two particles in series, and multiple particles under gravity are discussed. Finally, we present our concluding remarks in Sec. V.

2. Problem description

In this work, the sedimentation of reaction catalyst particles in the reactants are studied. During the process of catalyst settlement, the catalytic reaction of reactants takes place on the surface of the catalyst particles. Based on the coke deposition process, a simplified catalytic system is considered, and the reaction model can be described as

$$A \rightarrow B + Coke_{(s)} \tag{1}$$

This learning model assumes that: (1) both reactant and product are in the form of fluid phase; (2) the molar numbers of the reactant and product are essentially the same; and (3) the process is isothermal. With the reaction progresses, the concentration of reactants around the catalyst changes, which affects the reaction rate. In order to focus more on the consequences induced by coke deposition, that is, the change of reaction rate and particle mass, the heat of reaction is not considered in this work. Therefore, the sedimentation of catalyst particles is a couple of fluid flow, reactant advection–diffusion and the fluid–solid interactions. The reactive fluid flow is described by the Navier–Stokes equations together with the concentration advection–diffusion equation.

$$\frac{\partial \rho_f}{\partial t} + \nabla \bullet \left(\rho_f \boldsymbol{u}\right) = 0, \tag{2}$$

$$\frac{\partial \left(\rho_f \boldsymbol{u}\right)}{\partial t} + \nabla \bullet \left(\rho_f \boldsymbol{u}\boldsymbol{u}\right) = -\nabla p + \nabla \bullet \left(\mu \nabla \boldsymbol{u}\right) + \boldsymbol{F}, \tag{3}$$

$$\frac{\partial C_i}{\partial t} + \boldsymbol{u} \bullet \nabla C_i = D\nabla^2 C_i + J, \tag{4}$$

where $\boldsymbol{u}$, p, ρ_f denote macroscopic velocity, pressure and density of the fluid, μ and D are dynamic viscosity and diffusion coefficient, respectively. $\boldsymbol{F}$ is the body force term, and J is reaction source term related to catalytical reaction boundary conditions. By assuming the first-order reaction kinetics, the boundary conditions on the surface of catalysts are

$$\boldsymbol{u}(\boldsymbol{X}_\mathrm{b}, t) = \boldsymbol{U}_\mathrm{b}(\boldsymbol{X}_\mathrm{b}, t), \tag{5}$$

$$-D\frac{\partial C_r}{\partial n}(\boldsymbol{X}_\mathrm{b}, t) = J_{re}(\boldsymbol{X}_\mathrm{b}, t) = k_r C_r, \tag{6}$$

where $\boldsymbol{U}_\mathrm{b}$ is the desired velocity and J_{re} is the reaction mass flux on the particle surface. C_r is the solute concentration and k_r is the reaction rate constant of reactant.

In this work, we concentrated on the hydrodynamics of zeolite catalyst pellets in zeolite-catalyzed multi-phase reaction processes, which have been widely implemented in chemical industries. Typical examples include MTO, which bridges the synthesis of light olefins with coal and biomass resources, and FCC, which is the most important approach for gasoline production. Despite the practical significance of these processes, the hydrodynamics of industrial zeolite in fluid flows remains unclear. One of the most important features of these zeolite-catalyzed processes is that, during the reaction, large carbonaceous species, i.e. the so-called coke, are gradually formed inside the catalyst particles as retained product (Lin et al., 2022; Wang et al., 2022; Zhou et al., 2021). The coke formation could result in active site coverage, detrimentally reducing catalytic reaction activity of catalyst and eventually causing catalyst deactivation. As the reaction going on, the amount of coke deposited in the zeolites within catalyst pellets is gradually increased, and the catalytic reaction activity gradually decreases. Lower catalytic reaction activity of the catalyst, meanwhile, could reduce the formation rate of coke in catalyst pellets. Understanding such complicated interplay between the coke deposited in catalyst pellets and reaction activity of catalyst, as well as the consequence of hydrodynamics of catalyst in fluid flow in chemical reactors, remains a non-trivial task. Therefore, our current work aims at the effect

of coke deposition in catalyst, which is fundamentally altered by the reaction, on the motion of catalyst particles under reaction conditions. As far as we know, this is a topic yet to be explored.

In doing so, we assumed that the catalyst particles will be spheres with unchanged size and increased density in the reaction process as the coke deposition proceeds. This is justified as the coke species are essentially deposited in the micro- or nano-scale channels inside the catalyst pellets. However, the coke deposition not only influences the particle density, but also affects reaction rate. The former will lead to the change of motion of catalyst particle in the fluid flow, and the latter will change the coke deposition rate. In this regard, the deposition of coke could not be replaced by deposition of any other materials.

Despite that the catalyst particles are assumed as ideal solid spheres for simplicity, we believe this work initializes a learning model study on the complicated particulate two-phase flows for zeolite-based catalytic processes. Indeed, we argued that this learning model approach, at its preliminary stage, is mainly used to qualitatively understand the complex particulate reactive flows. Quantitative validation will be expected after this learning model is further improved by incorporating more details such as surface properties, temperature distribution, and zeolites amount of the catalyst pellets, which, however, remains the subject of our future research.

The reaction rate R with the activity decay is given as (Yang et al., 2021b; Zavarukhin and Kuvshinov, 2004):

$$R_r(\boldsymbol{r},t) = R_{coke}(\boldsymbol{r},t) = R_{max}{}^{*}a = k_r{}^{*}a{}^{*}C_r(\boldsymbol{r},t), \tag{7}$$

$$\frac{da}{dt} = -k_a R_{max}^2 m' a, \tag{8}$$

where R_{max}, a,m' and k_a are the reaction rate of fresh catalyst, catalytic activity, specific weight of coke deposited on the catalyst, and deactivation rate constant, respectively. The critical coke content of a catalyst is influenced by various factors such as the reaction mode, temperature, pore structure and surface chemical properties of the catalyst.(Wang et al., 2020; Zhao et al., 2018) In this work, it is assumed that the catalyst is deactivated when the amount of coke deposited in the particle reaches 25 % to balance the catalytic reaction and particle sedimentation. The overall variation in fluid density is much less than 1 %, which is negligible and can be considered a numerical error, therefore, the flow field can be treated as incompressible.

3. Numerical methods and validation

3.1. Immersed boundary-lattice Boltzmann method

A hybrid IB-LBM was used to solve the governing equations for the complex two-phase flow with mass diffusion in two-dimensional field. The velocity field was described by a two-dimensional nine directions (D2Q9) model $f_i(\boldsymbol{r},t)$ and the concentration field was solved by a two-dimensional five directions (D2Q5) model $g_i(\boldsymbol{r},t)$. For diffusion problems with surface geometry and Neumann boundaries, the D2Q5 model is more robust and accurate than the D2Q9 model for the CDEs when the convection is not very strong and the boundary effect is significant according to Li et al. (Li et al., 2017). The multiple-relaxation-time LB (MRT-LB) models are utilized. Compared with the Bhatnagar-Gross-Krook (BGK) model, MRT scheme has better stability and accuracy for the general convection–diffusion equations (CDEs) (Zhang et al., 2019). The corresponding lattice Boltzmann evolution equations for velocity field are given as

$$\begin{aligned} f_i(\boldsymbol{r}+\boldsymbol{e}_i\delta_t, t+\delta_t) - f_i(\boldsymbol{r},t) = & -\boldsymbol{M}^{-1}\boldsymbol{S}\left[m_i(\boldsymbol{r},t) - m_i^{eq}(\boldsymbol{r},t)\right] \\ & +\delta_t\boldsymbol{M}^{-1}\left(\boldsymbol{I}-\frac{\boldsymbol{S}}{2}\right)\boldsymbol{M}\boldsymbol{F}_i(\boldsymbol{r},t), \end{aligned} \tag{9}$$

$$m_i(\boldsymbol{r},t) = \boldsymbol{M}f_i(\boldsymbol{r},t), \tag{10}$$

$$m_i^{eq}(\boldsymbol{r},t) = \boldsymbol{M}f_i^{eq}(\boldsymbol{r},t), \tag{11}$$

where $f_i(\boldsymbol{r},t)$ is the density distribution function for velocity field at the space position $\boldsymbol{r}$ and time step t, $m_i(\boldsymbol{r},t)$ is the moment. $f_i^{eq}(\boldsymbol{r},t)$ is the equilibrium distribution function and $m_i^{eq}(\boldsymbol{r},t)$ is the corresponding equilibrium moment. $\boldsymbol{M}$ is the transformation matrix which is derived from discrete velocities using the Gram–Schmidt orthogonalization procedure. For the D2Q9 discrete velocity model, when the lattice speed satisfies $c = \delta_x/\delta_t = 1$, $\boldsymbol{M}$ can be chosen as

$$\boldsymbol{M} = \begin{pmatrix} 1 & 1 & 1 & 1 & 1 & 1 & 1 & 1 & 1 \\ -4 & -1 & -1 & -1 & -1 & 2 & 2 & 2 & 2 \\ 4 & -2 & -2 & -2 & -2 & 1 & 1 & 1 & 1 \\ 0 & 1 & 0 & -1 & 0 & 1 & -1 & -1 & 1 \\ 0 & -2 & 0 & 2 & 0 & 1 & -1 & -1 & 1 \\ 0 & 0 & 1 & 0 & -1 & 1 & 1 & -1 & -1 \\ 0 & 0 & -2 & 0 & 2 & 1 & 1 & -1 & -1 \\ 0 & 1 & -1 & 1 & -1 & 0 & 0 & 0 & 0 \\ 0 & 0 & 0 & 0 & 0 & 1 & -1 & 1 & -1 \end{pmatrix}, \tag{12}$$

$\boldsymbol{S}$ is the diagonal relaxation matrix in the moment space

$$\boldsymbol{S} = diag(1, s_\nu, 1.2, 1.15, 1, 1.15, s_\nu, s_\nu), \tag{13}$$

where s_ν is related to viscosity

$$s_\nu = \frac{1}{\frac{3\nu}{c^2\delta_t} + 0.5}, \tag{14}$$

For D2Q9, the lattice velocity vector $\boldsymbol{e}_i$ is given by

$$\boldsymbol{e}_i = \begin{cases} (0,0), & i = 0, \\ c\left(\cos\left[(i-1)\frac{\pi}{2}\right], \sin\left[(i-1)\frac{\pi}{2}\right]\right), & i \in \{1,2,3,4\}, \\ \sqrt{2}\,c\left(\cos\left[(2i-1)\frac{\pi}{4}\right], \sin\left[(2i-1)\frac{\pi}{4}\right]\right), & i \in \{5,6,7,8\}, \end{cases} \tag{15}$$

The corresponding equilibrium distribution function $f_i^{\mathrm{eq}}(\boldsymbol{r},t)$ is written as follows:

$$f_i^{\mathrm{eq}}(\boldsymbol{r},t) = \omega_{\mathrm{i}}\rho_f\left[1 + \frac{\boldsymbol{e}_i\cdot\boldsymbol{u}}{c_s^2} + \frac{(\boldsymbol{e}_i\cdot\boldsymbol{u})^2}{2c_s^4} - \frac{\boldsymbol{u}^2}{2c_s^2}\right], \tag{16}$$

where $c_s = 1/\sqrt{3}$. The weight of the i th direction ω_{i} is taken as

$$\omega_{\mathrm{i}} = \begin{cases} 4/9, & i = 0, \\ 1/9, & i \in \{1,2,3,4\}, \\ 1/36, & i \in \{5,6,7,8\}, \end{cases} \tag{17}$$

For the species transport and reaction, the concentration distribution function in the i th direction is denoted as $g_{\mathrm{i}}(\boldsymbol{r},t)$ and the evolution equation of the system is written as

$$\begin{aligned} g_i(\boldsymbol{r}+\boldsymbol{e}_i\delta_t, t+\delta_t) - g_i(\boldsymbol{r},t) = & -\boldsymbol{M}_g^{-1}\boldsymbol{S}_g\left[m_{g,i}(\boldsymbol{r},t) - m_{g,i}^{eq}(\boldsymbol{r},t)\right] \\ & +\delta_t\boldsymbol{M}_g^{-1}\left(\boldsymbol{I}-\frac{\boldsymbol{S}_g}{2}\right)\boldsymbol{M}_g\boldsymbol{J}_i(\boldsymbol{r},t), \end{aligned} \tag{18}$$

$$m_{g,i}(\boldsymbol{r},t) = \boldsymbol{M}_g g_i(\boldsymbol{r},t), \tag{19}$$

$$m_{g,i}^{eq}(\boldsymbol{r},t) = \boldsymbol{M}_g g_i^{eq}(\boldsymbol{r},t), \tag{20}$$

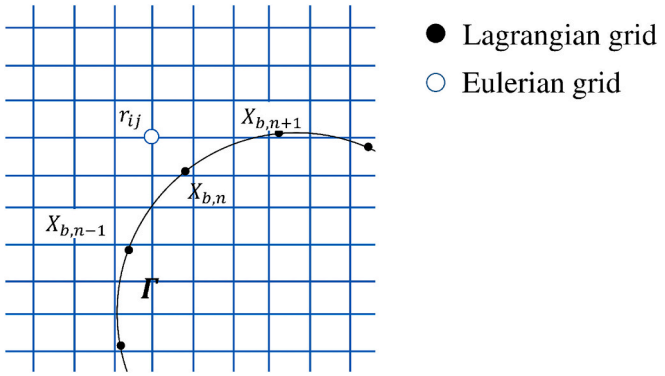

Fig. 1. Illustration of the Lagrangian grid and Eulerian grid of IBM.

The D2Q5 model was utilized with the transformation matrix $\boldsymbol{M}_g$ as

$$\boldsymbol{M}_g = \begin{pmatrix} 1 & 1 & 1 & 1 & 1 \\ 0 & 1 & -1 & 0 & 0 \\ 0 & 0 & 0 & 1 & -1 \\ 4 & -1 & -1 & -1 & -1 \\ 0 & 1 & 1 & -1 & -1 \end{pmatrix}, \tag{21}$$

$\boldsymbol{S}_g$ is the diagonal relaxation matrix in the moment space

$$\boldsymbol{S}_g = diag(1, s_D, s_D, 1, 1), \tag{22}$$

where s_D is related to diffusion coefficient

$$s_D = \frac{1}{\frac{3D}{c^2\delta_t} + 0.5}, \tag{23}$$

For D2Q5, the lattice velocity vector $\boldsymbol{c}_i$ is given by

$$\boldsymbol{c}_i = \begin{cases} (0,\ 0), & i = 0, \\ c\left(\cos\left[(i-1)\frac{\pi}{2}\right], \sin\left[(i-1)\frac{\pi}{2}\right]\right), & i \in \{1,2,3,4\}, \end{cases} \tag{24}$$

The corresponding equilibrium distribution function $g_i^{eq}(\boldsymbol{r}, t)$ is written as follows:

$$g_i^{eq}(\boldsymbol{r}, t) = j_i C_i \left[1 + \frac{\boldsymbol{c}_i \cdot \boldsymbol{u}}{c_s^2} + \frac{(\boldsymbol{c}_i \cdot \boldsymbol{u})^2}{2c_s^4} - \frac{\boldsymbol{u}^2}{2c_s^2}\right], \tag{25}$$

The weight of the i th direction j_i is taken as

$$j_i = \begin{cases} 1/3, & i = 0, \\ 1/6, & i \in \{1,2,3,4\} \end{cases} \tag{26}$$

The macroscopic velocity $\boldsymbol{u}$, density ρ_f and species concentration C_i of fluid flow can be calculated by

$$\rho_f = \sum_i^8 f_i, \tag{27}$$

$$\rho_f \boldsymbol{u} = \sum_i^8 \boldsymbol{e}_i f_i + \frac{\delta_t}{2}\boldsymbol{F}, \tag{28}$$

$$C_i = \sum_i^5 g_i + \frac{\delta_t}{2} J, \tag{29}$$

More details of the calculation process of MRT model can be found in the literature (Huang and Wu, 2014; Timm Krüger et al., 2017).

The moving boundaries of particles are treated using the Immersed Boundary method (IBM). The IBM describes the solid–fluid boundary curve $\boldsymbol{\Gamma}$ as a set of Lagrangian points that immersed in the fluid flow which is treated with the Eulerian points, as shown in Fig. 1. The interaction between the fluid flow and the particle boundary is imposed as the source terms $\boldsymbol{F}_b(\boldsymbol{r}, t)$ and $J_b(\boldsymbol{r}, t)$, which can be obtained by

$$\boldsymbol{F}_b(\boldsymbol{r}, t) = \sum_{\boldsymbol{\Gamma}} \boldsymbol{f}_b D_{ij}(\boldsymbol{r} - \boldsymbol{X}_b)\Delta s, \tag{30}$$

$$J_b(\boldsymbol{r}, t) = \sum_{\boldsymbol{\Gamma}} \delta J_b D_{ij}(\boldsymbol{r} - \boldsymbol{X}_b)\Delta s, \tag{31}$$

where $\boldsymbol{f}_b$ and δJ_b are the force density and mass source density on the Lagrangian point $\boldsymbol{X}_b$, respectively, and Δs is the arc corresponding to the Lagrangian point. The effects of $\boldsymbol{f}_b$ and δJ_b are diffused to the Eulerian fluid nodes through the $D_{ij}(\boldsymbol{x})$ which is a continuous kernel distribution function that approximates the delta function.

$$D_{ij}(\boldsymbol{r}_{ij} - \boldsymbol{X}_b) = \delta(x_{ij} - x_b)\delta\left(y_{ij} - y_b\right), \tag{32}$$

$$\delta(\Delta r) = \begin{cases} \frac{1}{8}\left(3 - 2|\Delta r| + \sqrt{1 + 4|\Delta r| - 4\Delta r^2}\right), & 0 \le |\Delta r| < 1, \\ \frac{1}{8}\left(5 - 2|\Delta r| - \sqrt{7 + 12|\Delta r| - 4\Delta r^2}\right), & 1 \le |\Delta r| < 2, \\ 0, & |\Delta r| \ge 2, \end{cases} \tag{33}$$

where x_b and y_b are the coordinates of Lagrangian point $\boldsymbol{X}_b$ on the particle surface, and x_{ij} and y_{ij} are the coordinates of the Eulerian point $\boldsymbol{r}_{ij}$. On the particle surface, non-slip boundary condition is adopted, and a direct-force scheme that has no free parameters is used

$$\boldsymbol{f}_b = 2\rho_f \frac{\boldsymbol{U}_b(\boldsymbol{X}_b, t) - \boldsymbol{u}^{noF}(\boldsymbol{X}_b, t)}{\delta t}, \tag{34}$$

$$\boldsymbol{u}^{noF}(\boldsymbol{X}_b, t) = \sum_{\boldsymbol{\Gamma}} \boldsymbol{u}^{noF}(\boldsymbol{r}, t) D_{ij}(\boldsymbol{r} - \boldsymbol{X}_b)\delta_x^2, \tag{35}$$

where $\boldsymbol{u}^{noF}$ is respectively the macroscopic velocity of the fluid flow without imposing the external source term.

For concentration field, due to the reaction process at the boundary, the influence of mass flux should be considered. δJ_b can be obtained by

$$\delta J_b = 2\left[J_{re}(\boldsymbol{X}_b, t) - \left(-D\frac{\partial C_i^{noE}}{\partial n}(\boldsymbol{X}_b, t)\right)\right], \tag{36}$$

where C_i^{noE} is respectively the macroscopic concentration of the fluid flow without imposing the external source term, and the concentration derivatives at Lagrangian point $\boldsymbol{X}_b$ could be calculated by(Rahman Nezhad and Mirbozorgi, 2018)

$$\frac{\partial C_i^{noE}}{\partial x}(\boldsymbol{X}_b, t) = \sum_{ij} \frac{\partial C_i^{noE}}{\partial x}(\boldsymbol{r}, t) D_{ij}(\boldsymbol{r} - \boldsymbol{X}_b)\delta_x^2, \tag{37}$$

$$\frac{\partial C_i^{noE}}{\partial y}(\boldsymbol{X}_b, t) = \sum_{ij} \frac{\partial C_i^{noE}}{\partial y}(\boldsymbol{r}, t) D_{ij}(\boldsymbol{r} - \boldsymbol{X}_b)\delta_x^2, \tag{38}$$

$$\frac{\partial C_i^{noE}}{\partial n}(\boldsymbol{X}_b, t) = \frac{\partial C_i^{noE}}{\partial x}(\boldsymbol{X}_b, t) \cdot \boldsymbol{n}_x + \frac{\partial C_i^{noE}}{\partial y}(\boldsymbol{X}_b, t) \cdot \boldsymbol{n}_y, \tag{39}$$

where $\frac{\partial C_i^{noE}}{\partial x}(\boldsymbol{r}, t)$ and $\frac{\partial C_i^{noE}}{\partial y}(\boldsymbol{r}, t)$ represent the derivatives of macroscopic concentration with respect to x and y at Eulerian point $\boldsymbol{r}_{ij}$. $\boldsymbol{n}_x$ and $\boldsymbol{n}_y$ are the components outward unit normal vector in the x and y directions on the Lagrangian point $\boldsymbol{X}_b$, respectively.

Note that $\boldsymbol{U}_b$ is the desired velocity on the particle surface

$$\boldsymbol{U}_b = \boldsymbol{V}_p + \boldsymbol{\omega}_p \times (\boldsymbol{X}_b - \boldsymbol{X}_p), \tag{40}$$

where $\boldsymbol{V}_p$ is the particle velocity, $\boldsymbol{\omega}_p$ is the angular velocity, and $\boldsymbol{X}_b - \boldsymbol{X}_p$ is the position vector of $\boldsymbol{X}_b$ based on the particle center $\boldsymbol{X}_p$.

The translational and rotational motion of the particles can be described by the Newton's Law.

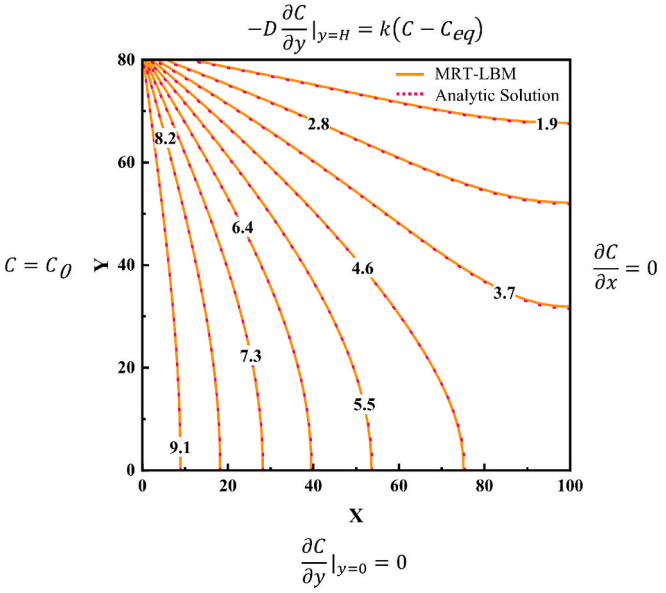

Fig. 2. Contour plot of reactant concentration in the rectangular region.

$$\frac{d(M_p \boldsymbol{V}_p)}{dt} = \boldsymbol{G} + \boldsymbol{F}_p + \boldsymbol{F}_{collis}, \tag{41}$$

$$\frac{d(\omega_p I_p)}{dt} = \boldsymbol{T}_p + \boldsymbol{T}_{collis}, \tag{42}$$

where M_p is the particle mass, I_p is the particle's moment of inertia tensor. $\boldsymbol{G}$, $\boldsymbol{F}_p$ and $\boldsymbol{T}_p$ are the force of gravity, the hydrodynamic force and torque exerted on the particle, respectively. $\boldsymbol{T}_{collis}$ is the torque due to the collision. The repulsive force $\boldsymbol{F}_{collis}$ is applied once the gap between two particles or between the particle and wall is less than a predefined threshold ξ, which is set as the grid size in this work. More specifically, for the collision between two particles, the force $\boldsymbol{F}^P_{collis}$ is modeled as (Glowinski et al., 2001; Feng and Michaelides, 2004)

$$\boldsymbol{F}^P_{collis} = \begin{cases} \frac{k}{\varepsilon}\left(\frac{||\boldsymbol{w}_P|| - (R_i + R_j) - \xi}{\xi}\right)^2 \frac{\boldsymbol{w}_P}{||\boldsymbol{w}_P||}, & ||\boldsymbol{w}_P|| \le R_i + R_j + \xi \\ 0, & ||\boldsymbol{w}_P|| > R_i + R_j + \xi \end{cases}, \tag{43}$$

where k is the scale factor of repulsive force, ε is the stiffness, and $\boldsymbol{w}_P = \boldsymbol{X}_i - \boldsymbol{X}_j$ is the distance vector between the center of particle i, $\boldsymbol{X}_i$, and that of particle j, $\boldsymbol{X}_j$. Note that R_i and R_j are the radius of particles i and j, respectively. Similarly, the repulsive force between a particle and wall is

$$\boldsymbol{F}^W_{collis} = \begin{cases} \frac{k}{\varepsilon}\left(\frac{||\boldsymbol{w}_W|| - 2R_i - \xi}{\xi}\right)^2 \frac{\boldsymbol{w}_W}{||\boldsymbol{w}_W||}, & ||\boldsymbol{w}_W|| \le 2R_i + \xi \\ 0, & ||\boldsymbol{w}_W|| > 2R_i + \xi \end{cases}, \tag{44}$$

where $\boldsymbol{w}_W = \boldsymbol{X}_i - \boldsymbol{X}_i'$ is the distance vector between the center of particle i and that of the image of particle i located symmetrically on the other side of the wall, $\boldsymbol{X}_i'$.

3.2. Model validation

3.2.1. Validation for reactive transport and fluid flow

Few studies have been so far conducted concerning the hydrodynamic behavior of catalyst particles with coke deposition at the particle scale, making it hard, if not impossible, to find suitable cases for verification. In this section, the in-home code was validated from both reaction–diffusion process and particle motion aspects by comparison with the analytical solutions and published numerical results. Firstly, a reaction–diffusion process in a rectangular region was simulated and the results were validated against an analytical solution (Kang et al., 2006). The rectangular region considered has the length of L and height of H with the mesh size of 100 × 80 lattice. A constant concentration is set at the left boundary ($x = 0$). The zero flux is set at the bottom ($y = 0$) and right boundary ($x = L$). A first-order reaction occurs at the top boundary ($y = H$), which can be expressed as

$$-D\frac{\partial C}{\partial y}|_{y=H} = k\left(C|_{y=H} - C_{eq}\right), \tag{45}$$

The analytical solution of the stable reaction–diffusion problem can be expressed as follows:

$$C(x,y) = (C_0 - C_{eq})\sum_{n=1}^{\infty} \frac{\sin(\beta_n H)}{N_n^2 \beta_n} * \frac{\cosh[\beta_n(x-L)]}{\cosh[\beta_n L]} \cos(\beta_n y) + C_{eq}, \tag{46}$$

$$N_n^2 = \frac{H}{2}\left(1 + \frac{\sin(2\beta_n H)}{2\beta_n H}\right), \tag{47}$$

$$(\beta_n H)\tan(\beta_n H) = \frac{kH}{D}, \tag{48}$$

Fig. 2 shows the contour plot of reactant concentration for reaction–diffusion in the rectangular region when the Damköhler number ($Da = kH/D$) takes 48. The simulation result is in excellent agreement with the analytical solution, and the relative global error $Err(C) = ||C_{exact} - C||_2 / ||C_{exact}||_2 \times 100\% = 1.65\%$, where C_{exact} and C are the concentration of the analytical solution and numerical results, respectively.

Then, to validate the code for reactive transport, the reaction flow around a circular particle (Molins et al., 2021) was simulated. In their work, Molins et al. used OpenFOAM-DBS to study the benchmark problem of a single reactive particle, in which a circular particle is placed in the center of a rectangular domain with the mesh size of 256 × 128. The top and bottom boundaries are assumed to be non-slip boundaries. The velocity inlet and pressure outlet are applied for the fluid flow at the left and right boundaries, respectively. The constant concentration and full development boundaries are applied for the solute transport at the left and right boundaries, respectively. An irreversible heterogeneous reaction of calcite dissolution occuring on the surface of particle was considered.

The simulation parameters are given in Table 1. When the system reaches the steady state, the distributions of $C(H^+)$ are shown in Fig. 3 (a). The pH values along the horizontal and vertical lines that cross the center of circular particle are given in Fig. 3(b) and (c). It can be found from the simulation results that for this reactive transport problem, the results of the D2Q5 model are more accurate than those of the D2Q9 model. The mean relative error for D2Q5 model of pH values along the

Table 1
Parameters for the simulations in case A, B and C.

Parameter	Symbol	Physical value	Lattice value
Fluid density	ρ_f	$1\,g/cm^3$	1
Kinematic viscosity	ν	$2 \times 10^{-2}\,cm^2/s$	0.13333
Diffusion coefficient	D	$2 \times 10^{-5}\,cm^2/s$	0.004
Length of domain	L	$0.1\,cm$	256
Width of domain	H	$0.05\,cm$	128
Grain radius	R	$0.01\,cm$	25.6
Inlet velocity	u_{in}	$0.12cm/s$	0.01875
Inlet concentration	c	$10^{-5}mol/cm^3$	0.01
Reaction rate constant	k	$10^{-1.05}cm/s$	0.1
Reynolds number	Re	0.6	
Peclet number	Pe	600	
Damköhler number	Da	178	

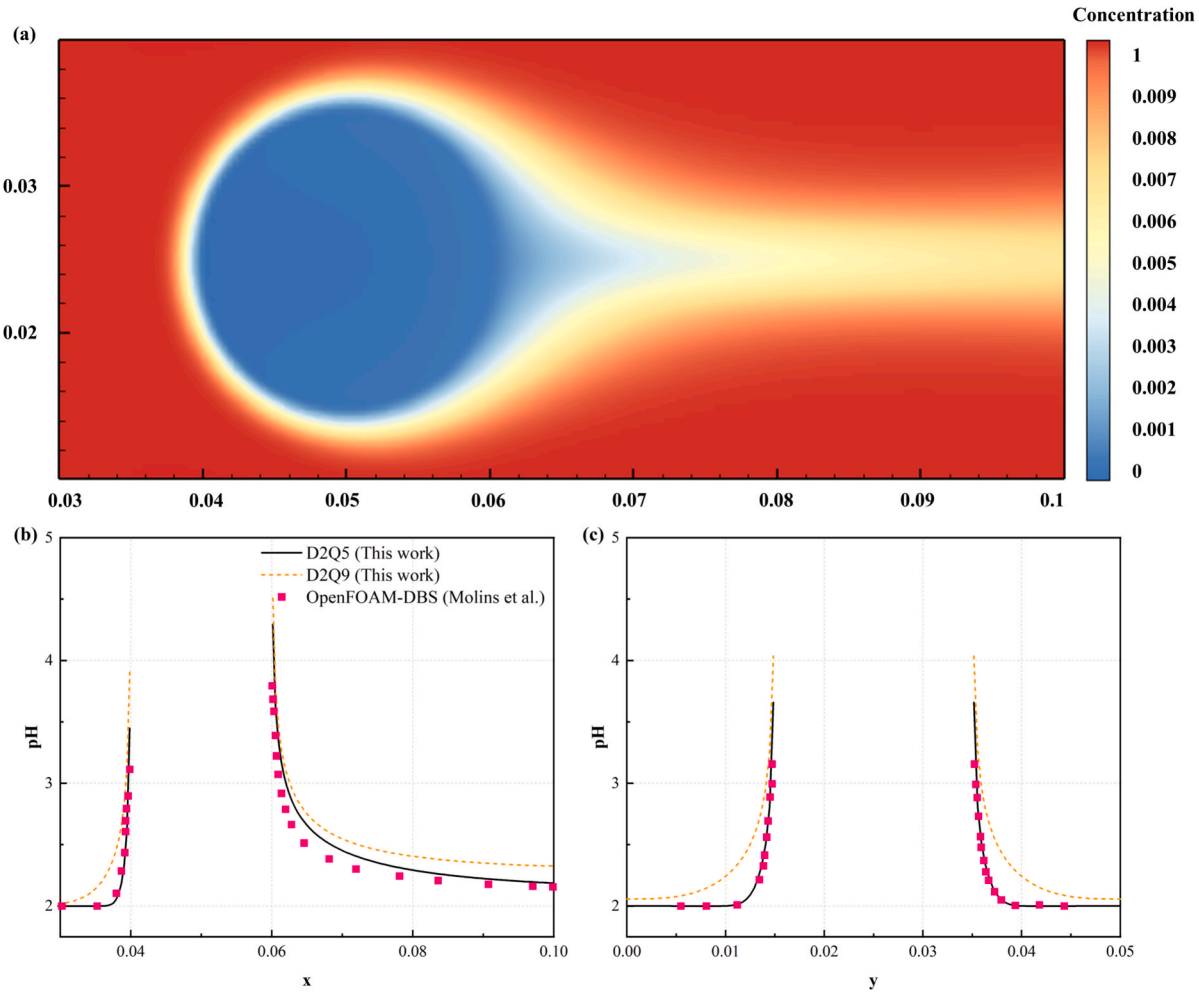

Fig. 3. The reaction flow around a circular particle: (a) the distribution of $C(H^+)$, (b) horizontal line, and (c) vertical line.

horizontal and vertical lines are 5.66 % and 2.05 %, respectively. For both of these cases, 50,000 steps were used to achieve the steady state (with relative error $< 10^{-6}$), consuming 0.7 h and 1.24 h of CPU time, respectively, by use of the Intel Xeon Gold 6132, 2.60 GHz respectively.

3.2.2. *The sedimentation of circular particle in Newtonian fluid*

To further verify our IB-LBM code for the case of moving particles, two benchmark problems studied extensively were simulated, i.e., the sedimentations of a single particle in a vertical channel and DKT process of two particles.

First, the grid independence was studied by simulating the settling of a circular particle in a vertical channel (Wan and Turek, 2006). The physical size of the computational domain is $L \times H = 2 \times 6cm$ and a circular particle with physical diameter $d_{p,phys} = 0.25cm$ and density $\rho_s = 1.25g/cm^3$ is initially located at $(1cm, 4cm)$. The density and viscosity of the fluid are $\rho_f = 1g/cm^3$ and $\nu = 0.1cm^2/s$, respectively. At $t = 0s$, the still particle starts to settle under gravity (the accelerating velocity $\boldsymbol{g} = 980cm/s^2$). To check the influence of grid size on the computational results, we implemented three grid unit sizes, i.e. 201×601, 251×751, and 301×901 are implemented, in which the particle diameter $d_p = 20$, 25, and 30 respectively in lattice units. Here the relation between physical particle diameter and its counterpart in lattice units is $d_{p,phys} = d_p \times \delta_x$, with δ_x being the lattice length. The instantaneous horizontal and vertical positions of the particle in three different grids are shown in Fig. 4. A good agreement can be observed between our results and that of Wan and Turek. According to Fig. 4, the results show that the computed results for various grid sizes are consistent. And for the two grids sizes of $d_p = 25$ and $d_p = 30$, the relative errors of particle Re are less than 1 %. Thus, $d_p = 25$ is chosen for saving computing resources and time in this work.

The second validation case is the sedimentation of two interacting circular particles settling in a channel, the so-called DKT problem which has been extensively studied by many researchers. The geometrical model and physical parameters in our validation follow the benchmark case reported by Feng et al.(Feng and Michaelides, 2004) The computational domain is $L \times H = 2 \times 8cm$. The particle density is $\rho_s = 1.01g/cm^3$, and the diameter is $d_p = 0.2cm$. The density and viscosity of the fluid are $\rho_f = 1g/cm^3$ and $\nu = 0.01cm^2/s$, respectively. Initially, the two particles are located at the channel centerline with a height of $7.2cm$ and $6.8cm$, respectively. Both particles and flow are set to be rest at $t = 0s$, and then the two particles settle under gravity. According to Fig. 5, the results show that the instantaneous vertical and horizontal positions of the two particles are almost consistent with the results in the literature (Feng and Michaelides, 2004; Jafari et al., 2011; Niu et al., 2006). Compared with the results of Nie et al., the average relative error in horizontal direction is 4.11 %. The instantaneous vorticity contours at different time stages are shown in Fig. 6, indicating that the DKT process has been successfully reproduced. The upper trailing particle is represented by the full line, while the lower leading particle is represented by the dash line. Before the collision, the simulation results are consistent with the literature. The tiny differences shown in the Fig. 6 during tumbling and subsequent separation processes can be attributed to the different particle–particle collision models. For the cases of single-particle and two-particle sedimentation, it took 1.81 h and 2.78 h of

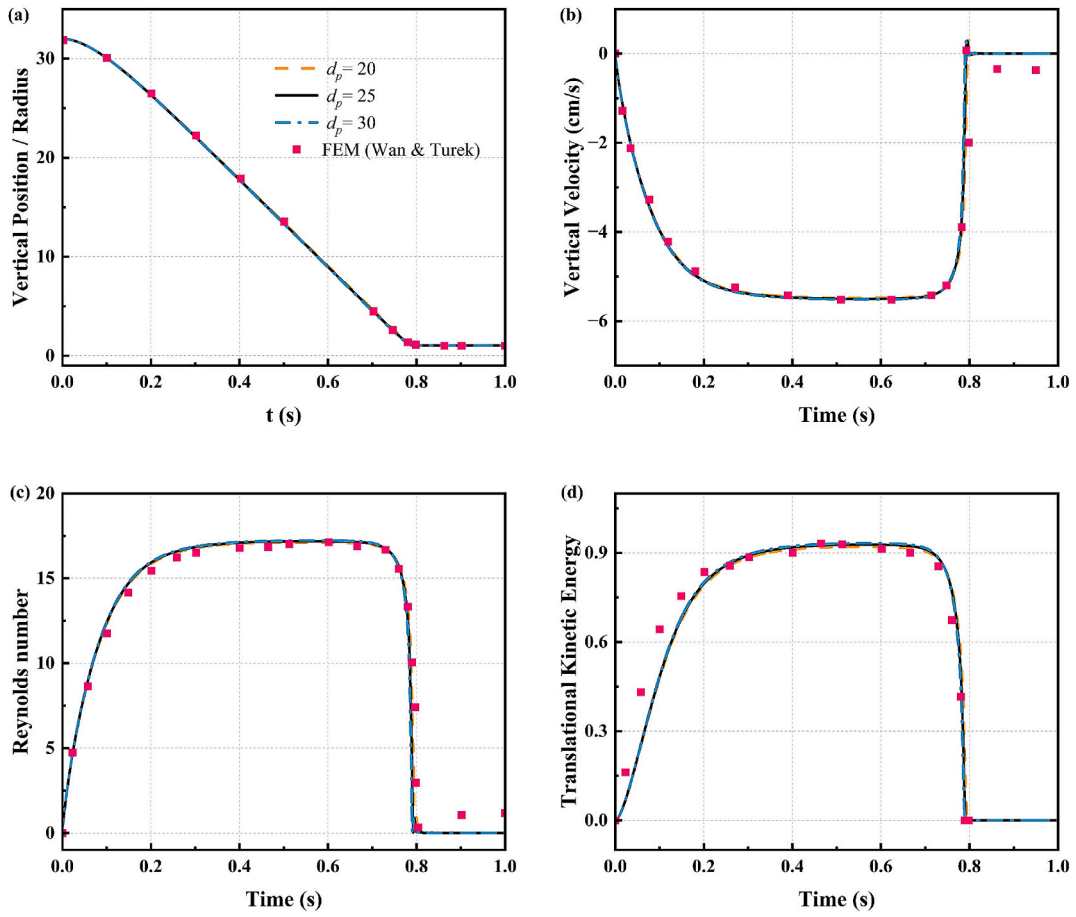

Fig. 4. Time history of grid independence of some quantities during sedimentation: (a) vertical position; (b) vertical velocity; (c) Reynolds number; (d) translational kinetic energy.

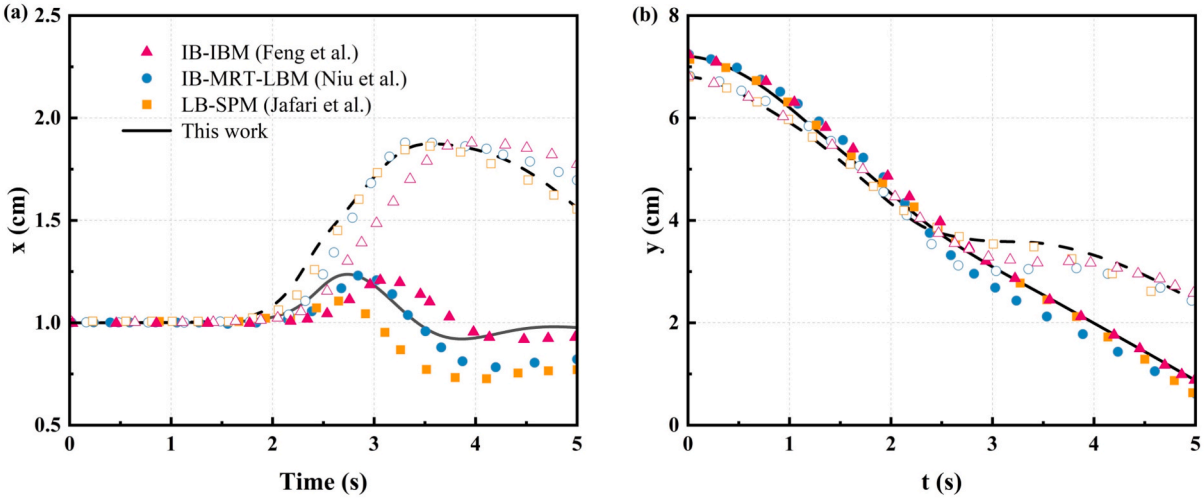

Fig. 5. Instantaneous position of two particles: (a) horizontal direction; (b) vertical direction.

CPU time respectively for $d_p = 25$ by use of the Intel Xeon Gold 6132, 2.60 GHz.

Through the aforementioned tests, it has been shown that our code can accurately simulate the reaction sedimentation process.

4. Results and discussion

In the heterogeneous catalytic reactor, there are usually many catalyst particles settling at the same time. It is important to research the interaction between particle–particle and particle–wall to reveal the sedimentation mechanism of catalyst particles. In this part, the complete settling process of catalyst particles from release to bottom in the reactor was captured. And the individual particle and multiple particles with different arrangements are simulated separately. The effects of coke deposition on particle motion and fluid–solid interaction were analyzed. In order to analyze the movement behavior and force of particles, the

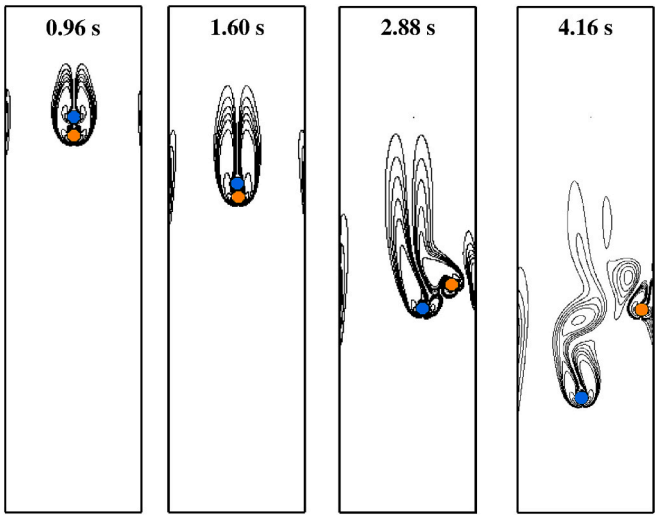

Fig. 6. Instantaneous vorticity contours at different time stages.

calculation domain of the same size is selected, the calculation domain with a lattice mesh size 251 × 1001 is selected for all of the following cases. The schematic of the sedimentation of one circular particle, two circular particles in parallel, and two circular particles in series are shown in Fig. 7(a), (b), and (c), respectively. For the convenience of description, the blue and orange particles are labeled as "Particle 1′" and "Particle 2′", respectively. Fig. 7(d) and (e) show the schematic of the sedimentation of five particles in a cruciform patter and a random pattern. For the convenience of later analysis, the particles are numbered by location. The simulation parameters refer to the validation

Table 2
Parameters for the simulations in case A, B and C.

Parameter	Symbol	Physical value	Lattice value
Particle diameter	d_p	$0.20\,cm$	25
Fluid density	ρ_f	$1\,g/cm^3$	1
Initial particle density	$\rho_{s,0}$	$1.01\,g/cm^3$	1.01
Length of domain	L	$2\,cm$	251
Hight of domain	H	$20\,cm$	2501
Kinematic viscosity	ν	$0.01\,m^2/s$	0.05
Diffusion coefficient	D	$0.0143m^2/s$	0.0714
Acceleration of gravity	g	$980\,cm/s^2$	0.012544
Reactant concentration of flow field	C_r	$0.01mol/cm^3$	1
Catalytic activity	a	0 1	
Reaction rate constant	k_r	$0.025\,cm/s$	0.001
Instantaneous Reynolds number	Re	$Re = \frac{\boldsymbol{u}d_p}{\nu}$	
Peclet number	Pe	0.7	
Ratio between distance from particle to channel centerline and distance from wall to channel centerline	d'	$d' = \frac{d}{L/2}$	

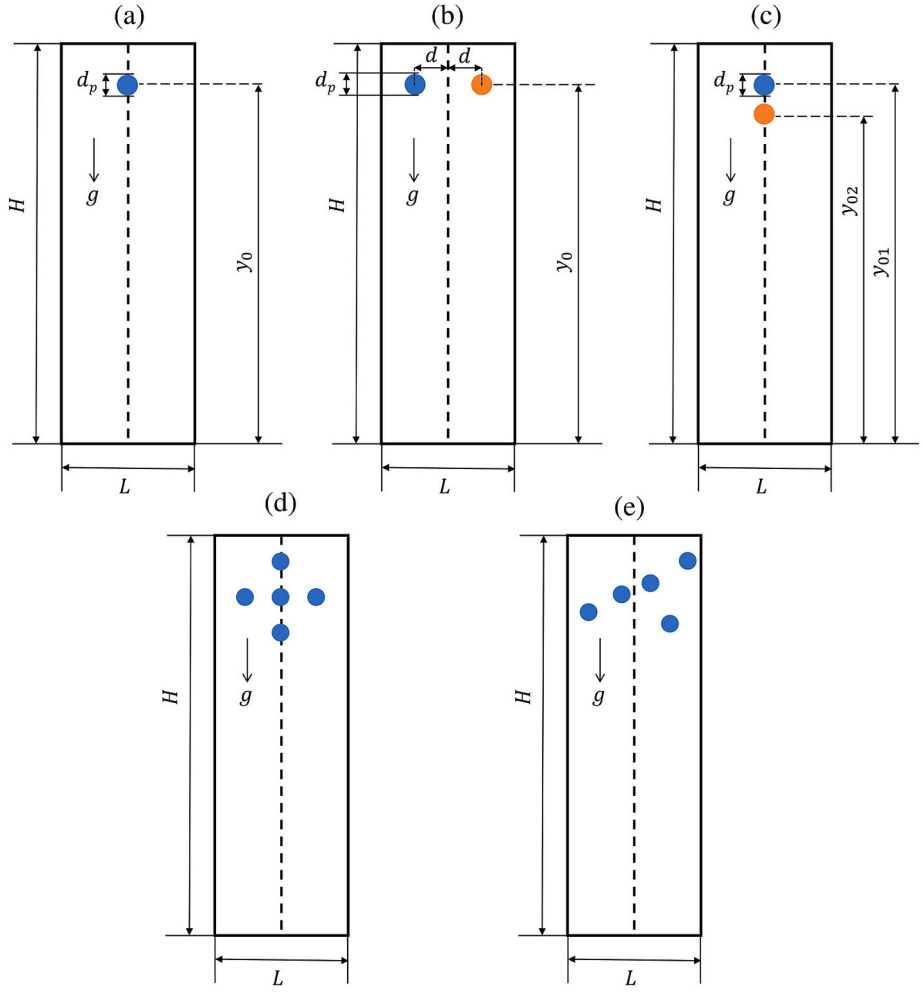

Fig. 7. The schematic of the sedimentation of (a) one circular particle; (b) two circular particles in parallel; (c) two circular particles in series; (d) five particles in a cruciform pattern; (e) five particles in a random pattern.

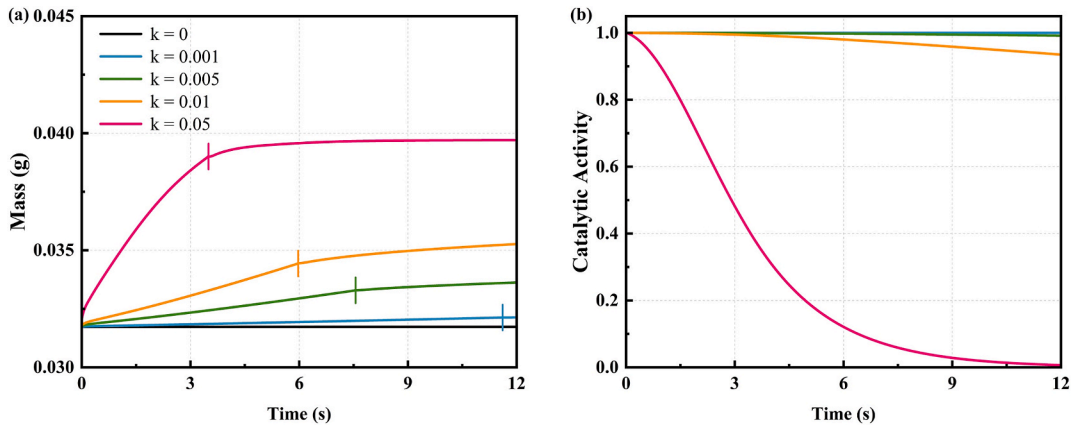

Fig. 8. The variation of (a) particles mass and (b) catalytic activity of a particle with time.

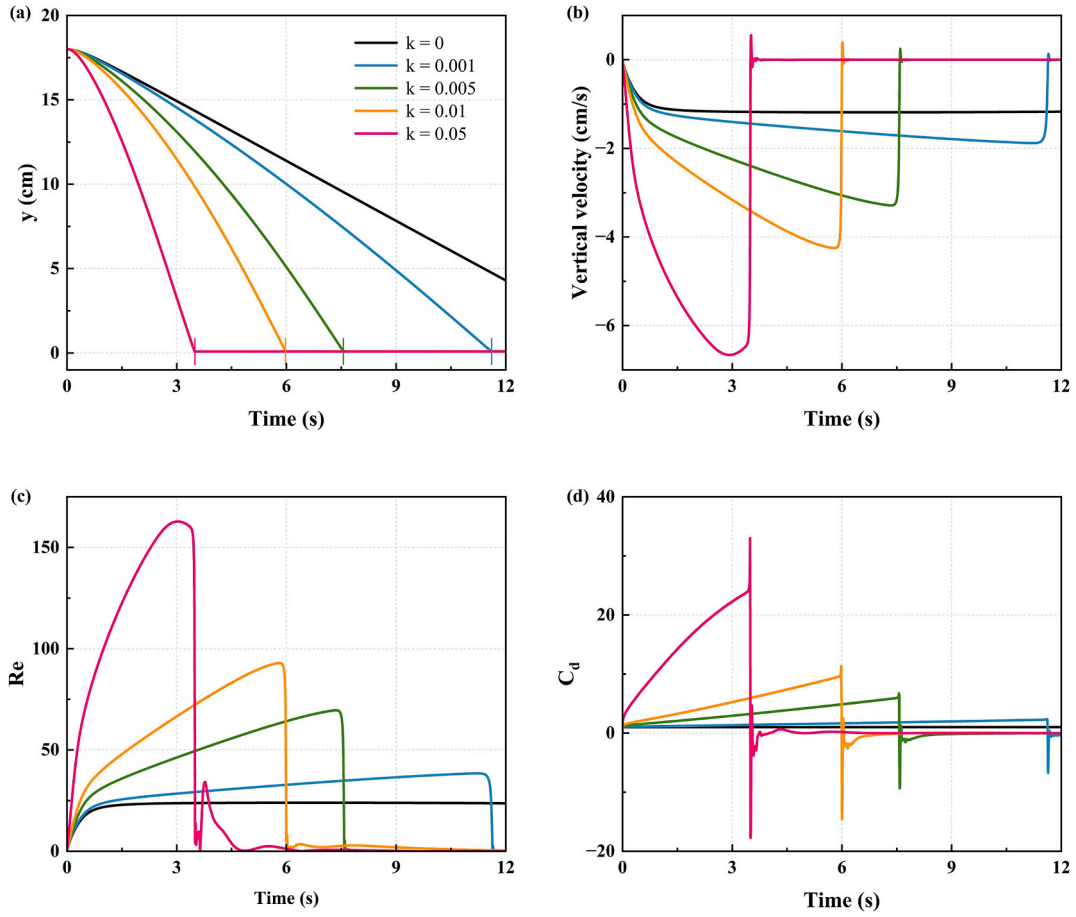

Fig. 9. The time history of some quantities of a particle during sedimentation: (a) vertical Position; (b) vertical velocity; (c) particle Reynolds number (d) drag coefficient.

in Section 3.2, as shown in Table 2.

4.1. *The settling of individual catalyst particle*

In the first case, the coke deposition on a single catalyst particle settling under gravity is studied. The particle is released in the channel from the initial position $(0.5L, 0.9H)$.

The evolution of mass and catalytic activity of individual catalyst particle with time for various k is illustrated in Fig. 8. It can be seen that coke formation influences the activity of the catalyst. The catalytic activity declines over time because of the continuous accumulation of coke. By comparing the results with different reaction rate constants, it can be found that higher coke deposition rate is achieved with an increasing reaction rate, leading to the rapid deactivation. Once the particle hit the bottom, which are represented by the symbol " | " in Fig. 8a, the concentration of reactants in the surrounding flow field decreases due to continuous reactions, as a result, slowing down the reaction rate. It can be seen that when $k \neq 0$, an inflection point can be found at the time when the particle hits the bottom, as marked in Fig. 8a.

Fig. 9 shows the temporal changes in vertical position, vertical

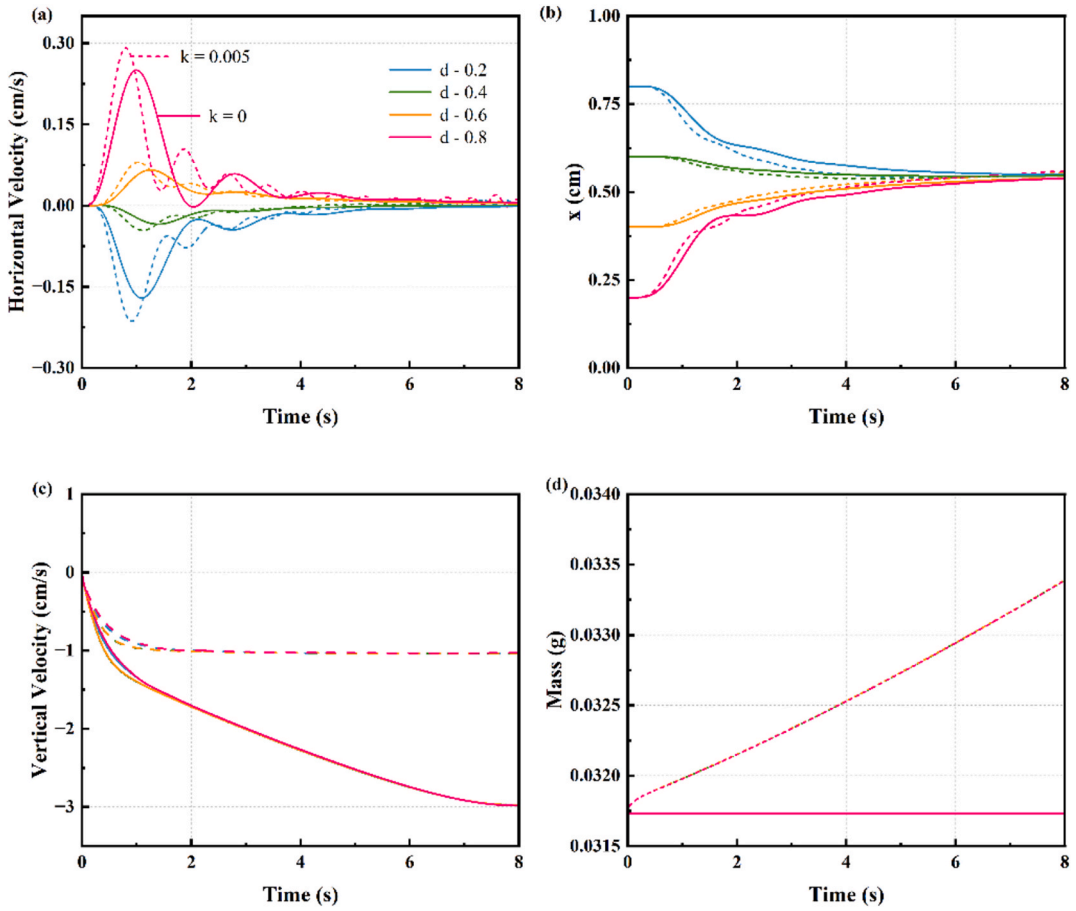

Fig. 10. The time history of some quantities of particles during sedimentation where the solid line represents inert particle and the dash line represents the catalyst particle: (a) horizontal velocity; (b) horizontal position; (c) vertical velocity; (d) particles mass.

velocity, Reynolds number, and drag coefficient of single particle during sedimentation under various k. For an inert particle, it accelerates under gravity, and the drag force increases until the particle reaches its steady state. While for catalyst particle, during the sedimentation process, the particle density and the corresponding gravity increase with coke formation, leading to a persistent imbalance of forces that prevents the attainment of the final settling velocity. The larger the reaction rate, the greater the increase in particle settling velocity.

4.2. The settling of two catalyst particles in parallel

The sedimentation of two catalyst particles in parallel within a channel is investigated. The dimensionless position represents the ratio of the distance between the particle position and the channel centerline to half of the channel width, which is $d' = d/L/2$. Particle 1 and Particle 2 are released from the initial position $(0.5L - 0.5d'L,\ 0.9H)$ and $(0.5L + 0.5d'L, 0.9H)$ at the same horizontal height.

The influence of the proximity of two particles are investigated. The dimensionless position $d' = 0.2, 0.4, 0.6,$ and 0.8 are chosen to illustrate the influence of initial position on the hydrodynamic behavior of catalyst particles. Different from single particle sedimentation, there exist particle–particle and particle–wall interaction forces in the horizontal direction for two particles sedimentation in parallel. As shown in Fig. 10 (a), the horizontal velocities of both inert particles and catalyst particles with $k = 0.005$ eventually tend to zero, which indicate that the inertial focusing behavior occurs. As shown in Fig. 10(b), the equilibrium position for the catalyst particle is closer to the channel centerline compared to that for the inert particle. In contrast, the influence of proximity on the vertical sedimentation is relatively small as shown in Fig. 10(c). The particles with the moderate initial position have a relatively large vertical velocity. As further can be seen from Fig. 10(d), the influence of initial position on coke deposition can be negligible. Therefore, to investigate the effect of reaction rate on the motion of catalyst particles, the initial dimensionless position $d' = 0.2$ is chosen for the analysis, i.e., the two particles are relatively close to each other. The reaction rate constants are set as 0.001, 0.005, 0.01, and 0.05, respectively.

As illustrated in Fig. 11(a), in the vertical direction, the larger the reaction rate, the earlier the particle hits the bottom, and the vertical velocity of two particles in parallel is in fact lower than that of a single particle settling. From Fig. 11(b), it can be found that the horizontal movement of particles can be divided into three stages. The analysis is combined with the Re shown in Fig. 11(c) and lift coefficient of Particle 1 shown in Fig. 11(d), which can be expressed as $C_l = 2F_x/A_p\rho_l u^2$. The first stage is the moment of initial release. Fig. 12 shows the instantaneous contour plots of velocity at $t = 0.16s$. Due to the small spacing between particles, the interaction between particles is dominant. The liquid velocity gradient on the right side of the particle is higher than that of the left side due to the right particle effect, which results that the lift force is to the left and particles are separated from each other. With the increase of k, the distance between the two particles increases due to the influence of concentration gradient in the surrounding concentration field. Then, in the second stage, the movement of catalyst particles with different k is different, the instantaneous vorticity contours are shown in Fig. 13. For $k = 0$ and $k = 0.001$, the lift force acting on the particle is approximately zero, so the particles remain constant horizontal position until they hit the bottom. When $k \geq 0.005$, the Re of Particle 1 exceed 47 during sedimentation, as shown by the marked points in the Fig. 11(c).

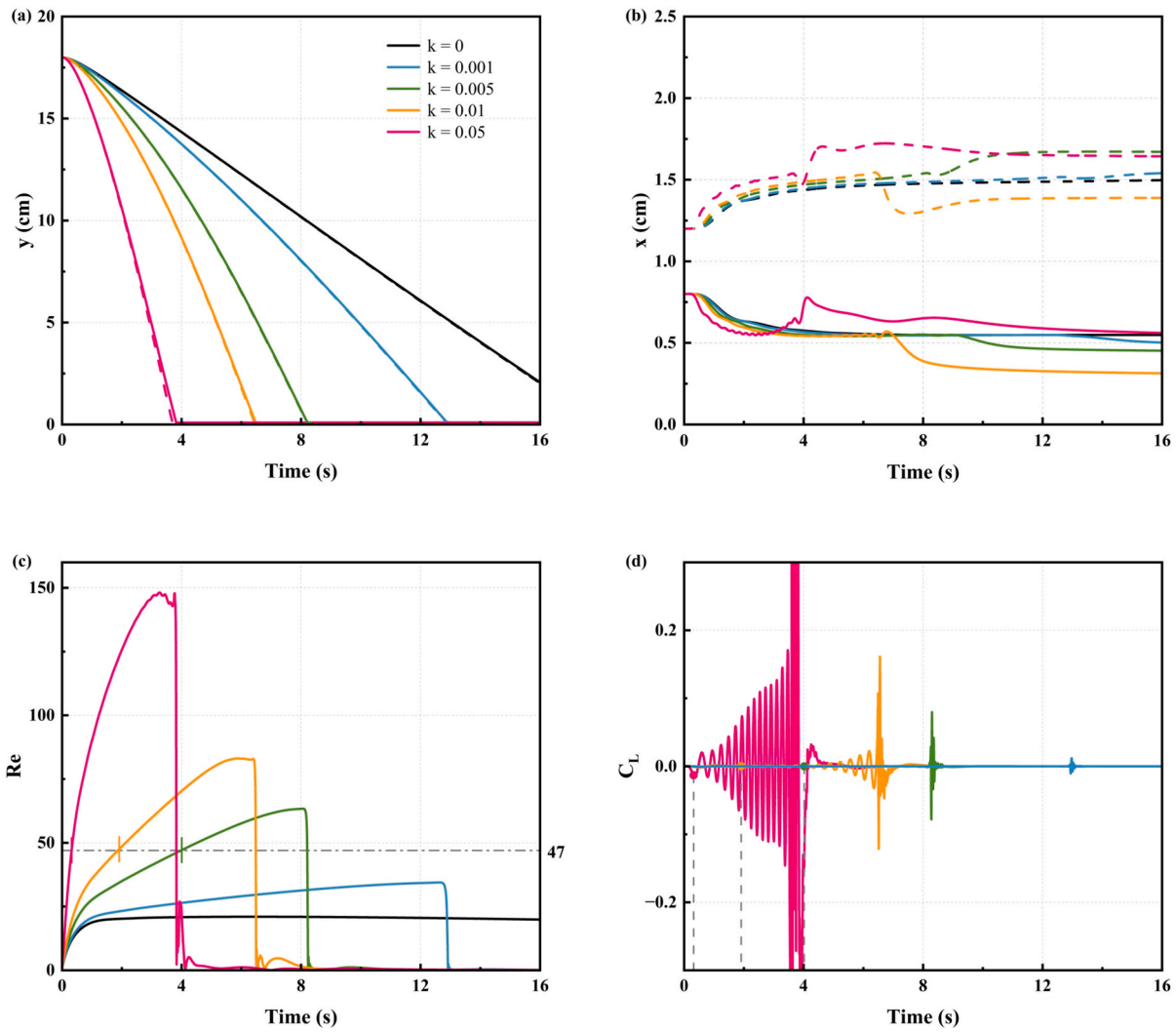

Fig. 11. The time history of some quantities of particles during sedimentation where the solid line is Particle 1 and the dash line is Particle 2: (a) vertical position; (b) horizontal position (c) Reynolds number; (d) lift coefficient.

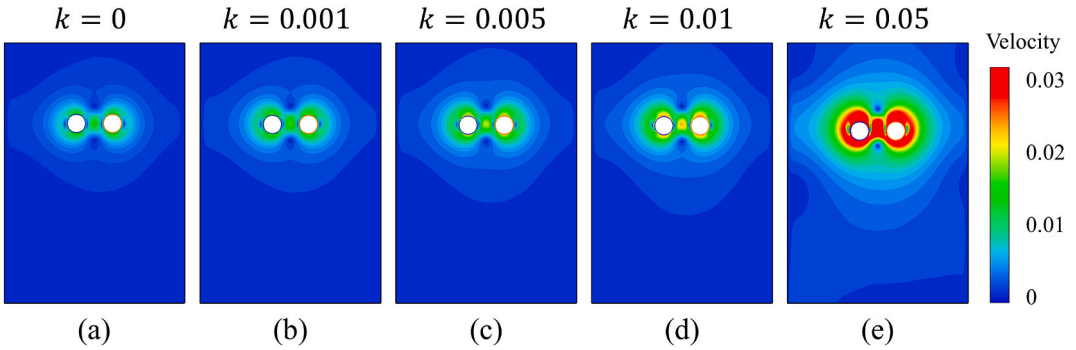

Fig. 12. Instantaneous contour plots of velocity at $t = 0.16s$, with (a) $k = 0$; (b) $k = 0.001$; (c) $k = 0.005$; (d) $k = 0.01$; (e) $k = 0.05$.

At that time, the particle vortex is asymmetrical, and there are small disturbances in the lift force and horizontal position. This observation of vortex shedding phenomenon in catalyst particles sedimentation is analogy to the that in fluid flow past a solid cylinder. In the latter, however, the asymmetrical tail vortex occurs at a certain *Re*, and the Karman vortex street appears as *Re* is higher than this critical value. Base on this, we can hypothesize that in the sedimentation process with chemical reaction, there also exists such a reaction rate related critical *Re*, beyond which the vortex shedding occurs. However, a theoretical formula to predict this critical *Re* is yet to be further established in a future research work. The third stage is a period of time before and after the particles hit the bottom. The interaction between particle and fluid flow plays a significant role. For $k = 0.001$ and $k = 0.005$, when the particle hits the bottom, the *Re* of Particle 1 increases to 34 and 63, respectively. As there is no vortex shedding occurred, the two particles constantly move away from each other due to the influence of

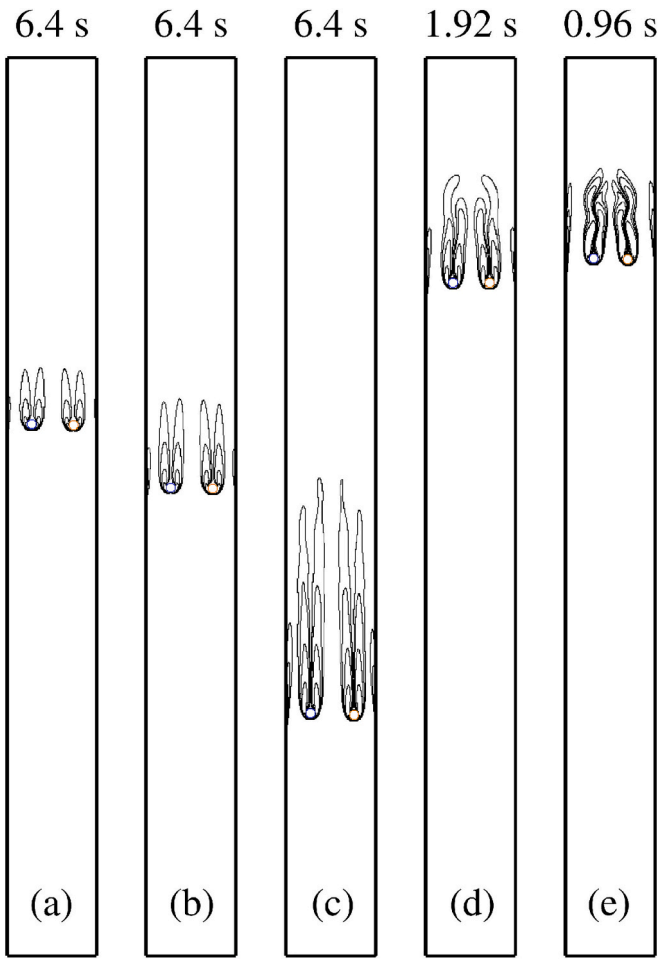

Fig. 13. Instantaneous vorticity contours at the second stage, with (a) $k = 0$; (b) $k = 0.001$; (c) $k = 0.005$; (d) $k = 0.01$; (e) $k = 0.05$.

concentration gradient. However, catalyst particles with a large reaction rate constant exhibit different moving behavior. For $k = 0.01$ and $k = 0.05$, the *Re* of Particle 1 increases to 83 and 148, respectively, with vortex shedding. The vortex around the particles could transfer additional energy to the fluid. Owing to the fluid disturbance, the motion of particles in the third stage is different under two reaction rates. With the gradual dissipation of kinetic energy, particle motion is once again dominated by the influence of solute diffusion. The analysis is carried out in combination with the instantaneous contour plots of reactant concentration, as shown in Fig. 14.

Fig. 15 compares the difference of coke deposition in the sedimentation of individual particle deposition and two particles in parallel. The dotted line indicates the weight of carbon deposited by a single particle, and the dot marks the time of hitting the bottom. The solid line represents the weight of coke deposited in Particle 1, the short dot line represents Particle 2, and the bottoming time of two particles are represented by the symbol " | ". While the dash line is the weight of coke deposited in a single particle, and the time of hitting the bottom is

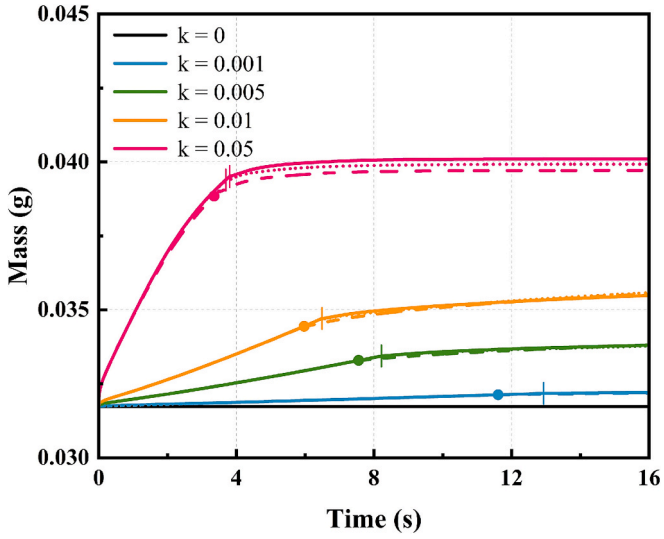

Fig. 15. The variation of particles mass with time.

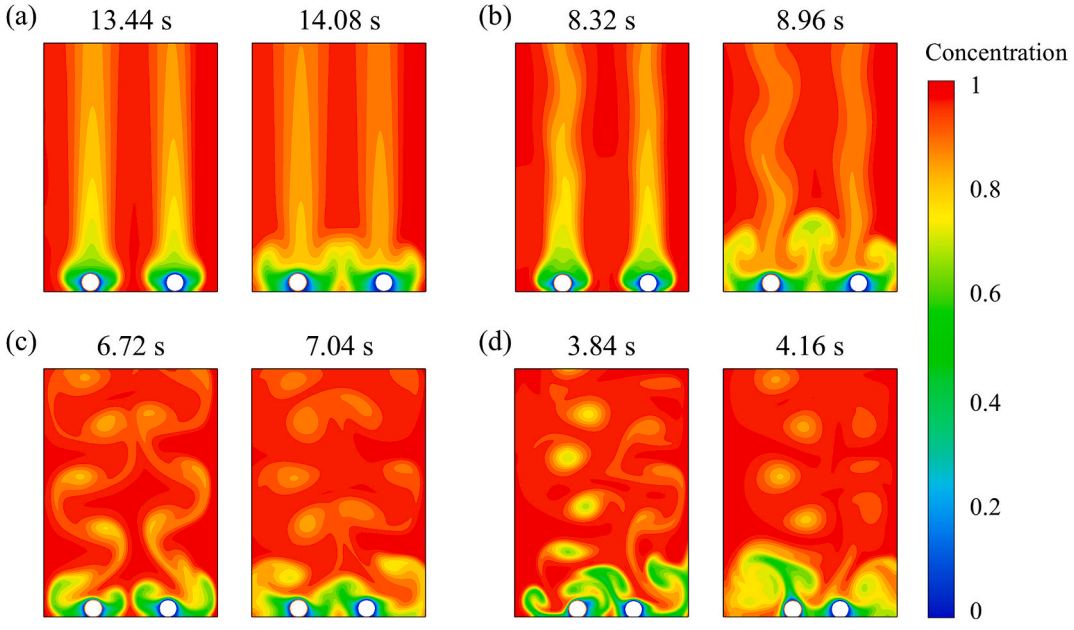

Fig. 14. Instantaneous contour plots of reactant concentration when the two particles hit the bottom, with (a) $k = 0.001$; (b) $k = 0.005$; (c) $k = 0.01$; (d) $k = 0.05$.

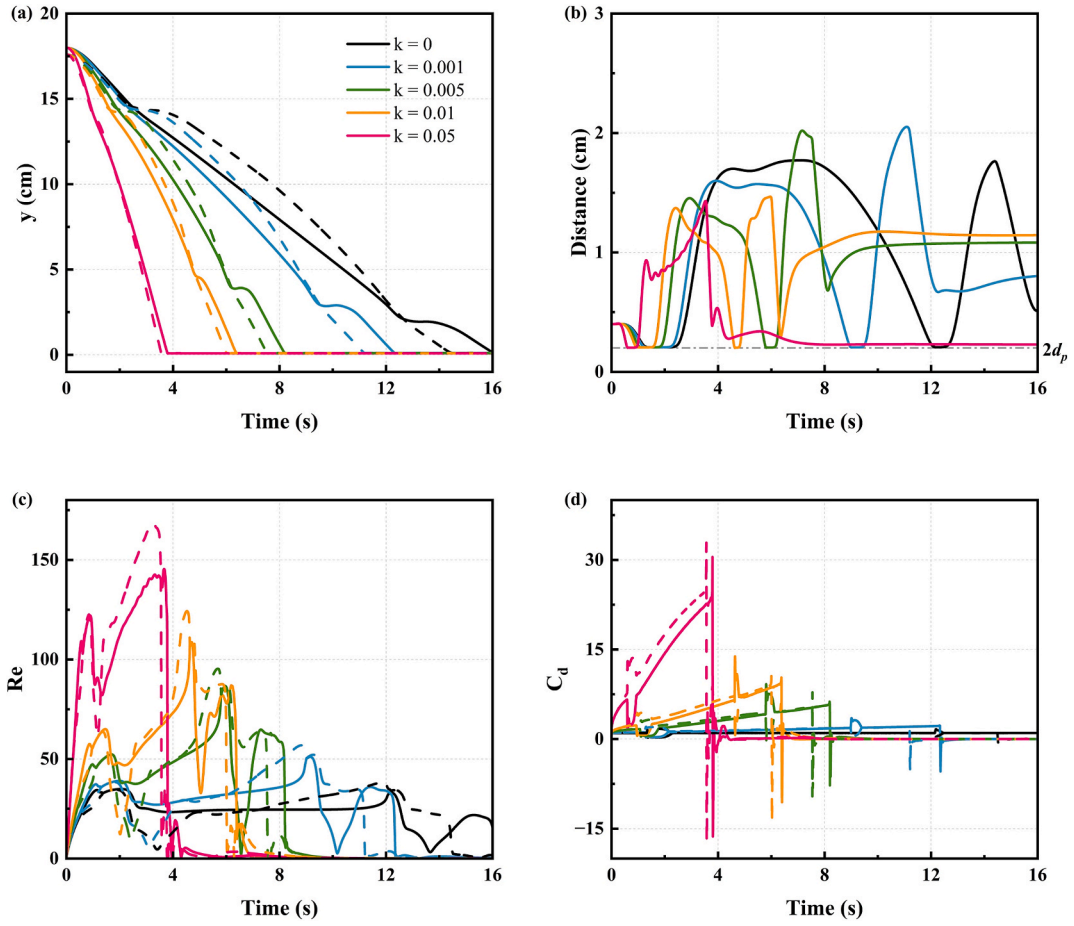

Fig. 16. The time history of some quantities of particles during sedimentation where the solid line is Particle 1 and the dash line is Particle 2: (a) vertical position; (b) distance between the centers of the two particles; (c) Reynolds number; (d) drag coefficient.

marked with the symbol "●". According to the above analysis, compared with the individual particle, the parallel settling particles hit the bottom later, so more coke can be deposited. However, the two particles in parallel do not interact vertically, and they take almost the same time to hit the bottom, leading to a similar amount of coke deposition.

4.3. The settling of two catalyst particles in series

In this case, we simulate the DKT of two catalyst particles in series and compare the dynamic behavior of particles with different reaction rates to investigate the influence of coke deposition on the vertical motion process. Dynamic behavior effects on the reaction are also analyzed. Particle 1 and Particle 2 are released in the channel from the initial position $(0.5L, 0.9H)$ and $(0.5L, 0.9H-2d_p)$ at $t = 0s$.

Fig. 16 shows the vertical position, distance between the centers of the two particles, *Re* and the distance between the centers of two particles. It can be seen that the reaction has a great influence on the particle movement. Under the conditions of a low reaction rate constant $(k < 0.05)$, the Particle 2 creates a wake of low pressure. When Particle 1 moves into this area, the drag force decreases, and then accelerates to fall and collide. The chemical reaction enlarges the area of the low-pressure zone, further accelerating the particle fall process. Fig. 16(a) and (b) show that the larger the k, the earlier the next DKT process occurs. When $k = 0.05$, the reaction rate constant is relatively large. Compared to the inert particles, the *Re* of the particles increases from 33

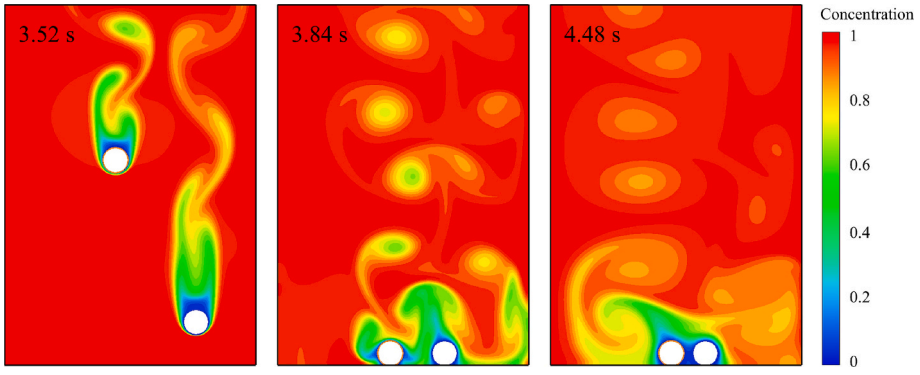

Fig. 17. Instantaneous contour plots of reactant concentration when the two particles which $k = 0.01$ hit the bottom.

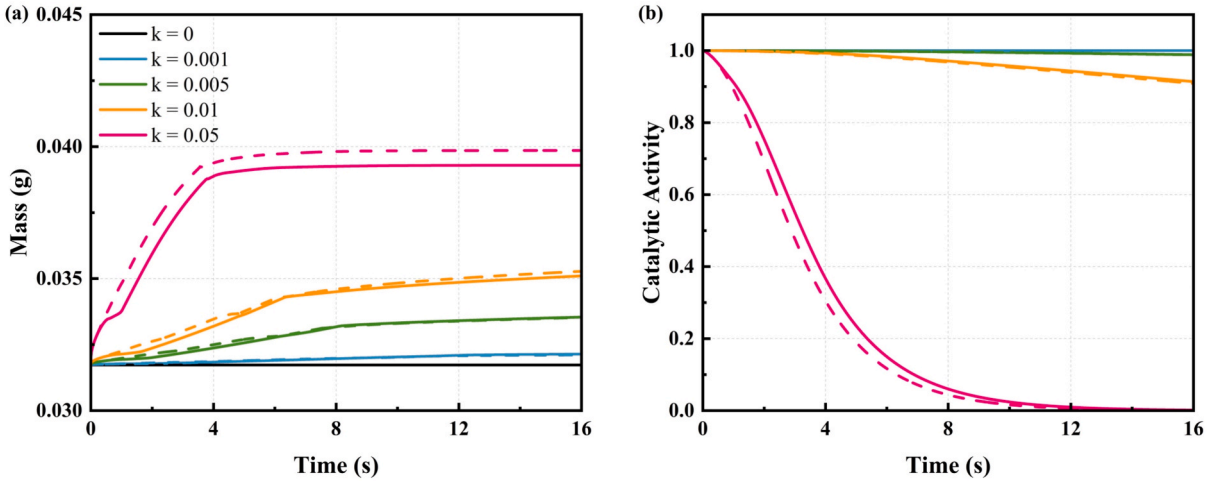

Fig. 18. The variation of (a) particles mass and (b) catalytic activity of two catalyst particle with time.

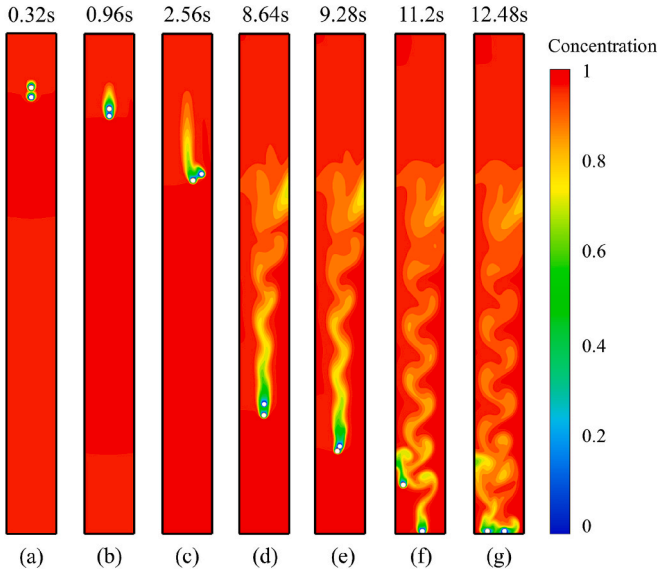

Fig. 19. Instantaneous contour plots of reactant concentration with $k = 0.001$ at characteristic time.

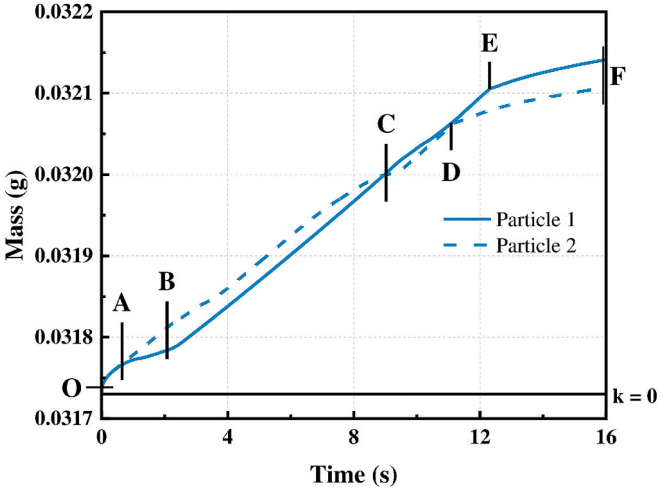

Fig. 20. The variation of particles mass with $k = 0.001$ with time.

to 108 during the first collision, as shown in Fig. 16(c). At this time, the significant disturbance of the surrounding flow field affects the movement direction of particles. The two particles move away from each other, and the DKT process no longer takes place. After the two particles hit the bottom, they approach each other under the influence of the concentration gradient and maintain a certain distance, as shown in Fig. 16(b) and Fig. 17.

By comparing the mass changes of two particles during sedimentation as shown in Fig. 18, it can be seen that the motion of particles also affects the deposition of coke. For two catalyst particles in series, the deposition of coke is not uniform, resulting in the heterogeneous coke deposition rate and catalytic activity. Fig. 19 and Fig. 20 present the detailed motion and coke deposition process of each particle under the reaction rate constant of $k = 0.001$ as an example. As shown in Fig. 20, there are several characteristic points appearing in particle mass variation, with each corresponding to a subfigure in Fig. 19. The consumption of reactants creates a concentration gradient around the particles, and the movement of particles alters the concentration distribution of the reactants in the surrounding flow field, thereby affecting the speed of the chemical reaction. From the beginning time O until time A, the concentration field around the two particles remains constant, as shown in Fig. 19(a), and the coke is deposited in the particles at a consistent rate. From time A to time B, Particle 1 enters the wake of Particle 2, as shown in Fig. 19(b), and the surrounding concentration of Particle 1 is relatively low, causing the reaction rate to slow down. Until the two particles collide at time B, Particle 1 rolls to the front end of Particle 2. After this point, the concentration field around Particle 1 is no longer influenced by Particle 2, as shown in Fig. 19(c), leading to an increase in the reaction rate. Fig. 19(d) shows the second drafting process, which takes place from time B to time C. At time C, it can be seen from Fig. 19(e) that the second collision occurs, causing a change in the positions of the two particles and a subsequent change in the reaction rate. As a result, the two particles move farther away, and the concentration field of any particle is less influenced by its counterpart. Particle 2 and Particle 1 hit the bottom at times D and E, respectively, and the corresponding contour plots of reactant concentration are shown in Fig. 19(f) and (g), respectively. In consequence, the concentration field around these two particles is evenly distributed and lower than the initial concentration field, as a result, the reaction rate decreases.

4.4. *The settling of five catalyst particles*

From the above analysis, it can be seen that chemical reactions can affect the movement of particles and the interaction between fluids and solids. In chemical reactor such as a fluidized bed, the chemical reaction

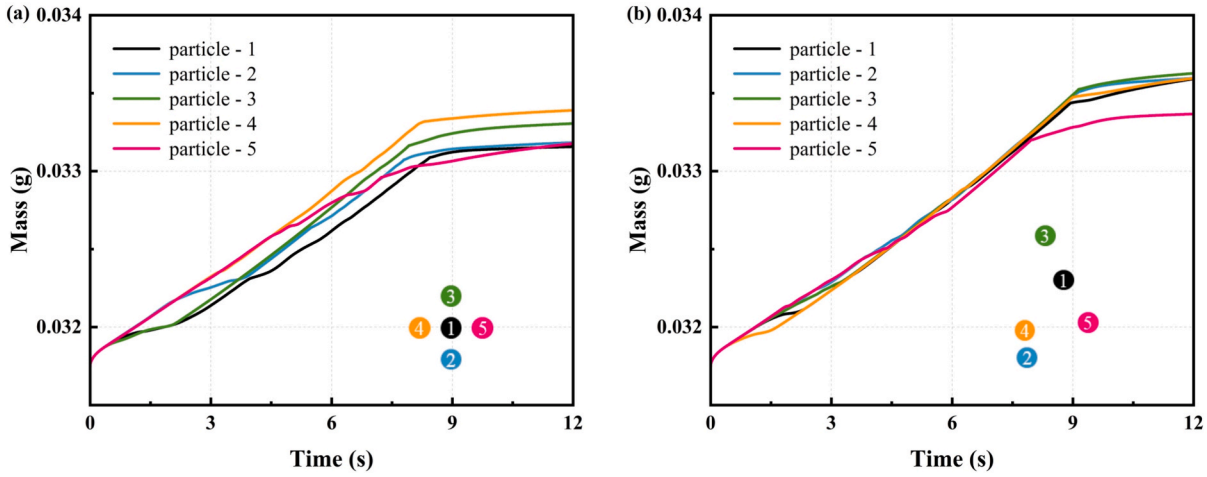

Fig. 21. The variation of particles mass with time at different initial release locations (a) cruciform pattern; (b) random pattern.

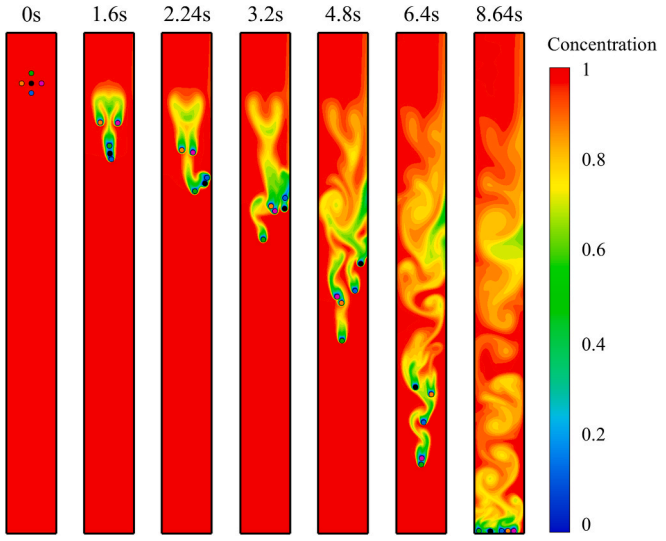

Fig. 22. Instantaneous contour plots of reactant concentration in a cruciform pattern at characteristic time.

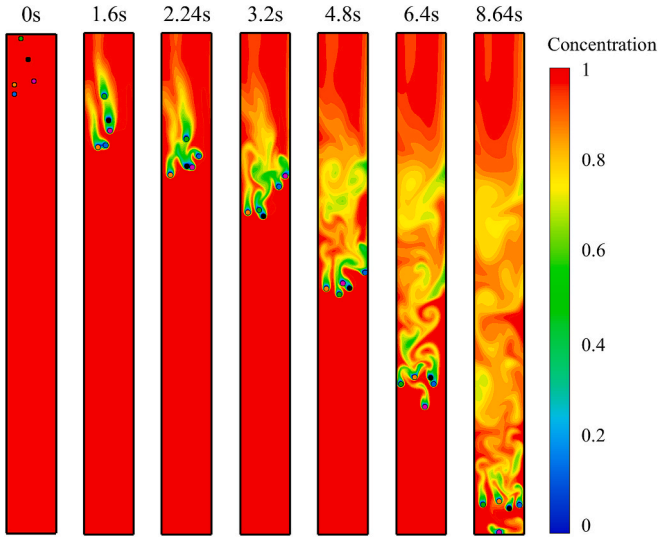

Fig. 23. Instantaneous contour plots of reactant concentration in a random pattern at characteristic time.

and multiple particle motion must be considered simultaneously. To further investigate the relationship between chemical reaction and the motion of multiple particles, we simulated the sedimentation of five catalyst particles with a moderate reaction rate of $k = 0.005$. The initial release positions are distributed in a cruciform pattern and a random pattern, respectively.

Fig. 21 shows the change of particle mass over time for two initial arrangements. Compared with previous studies, as particle number increases, the wall constraint becomes more severe, and the average settling velocity in the vertical direction is suppressed. The weight of coke deposited on the particles is largely influenced by the initial arrangement. For these two configurations, the trajectories of particle motion are quite different as shown in Figs. 22 and 23, resulting in the varying concentration distribution around the particles, which ultimately affects the reaction rate.

Fig. 22 shows the instantaneous contour plots of reactant concentration for the cruciform pattern, where Particle 1 is released in the channel from the initial position $(0.5L, 0.9H)$, and other particles are 2 d_p away from particle 1 along the Cartesian coordinate system. It can be seen that after the initial release, Particles 1 and 3, under the influence of Particle 2, have a significantly lower concentration of surrounding flow field than other particles, resulting in a lower coke deposition rate. After the first kissing, Particle 3 tumbles to the front and then maintained this advantage, having the fastest reaction rate. After the particles hit the bottom, the concentration field around the particles are lower than the initial concentration field, as a result, the reaction rate decreases.

For the random pattern, particles' initial positions are randomly distributed in the upper 85 % of the channel. In this randomly generated case, the initial distribution of particles is more centralized in the left half of the channel. As shown in Fig. 23, compared to the case in a cruciform pattern, the average settling velocity in the vertical direction is much smaller, where the collision occurs more times during the sedimentation. Due to the longer fall time, more coke is deposited in the particles.

Overall, quite different motion of particles with different initial position can be observed due to the complicated particle–particle and particle–wall interaction. This results in the nonuniform reaction and thus the heterogeneity of coke deposition in catalyst particles even within the same reactor. Understanding the motion and deactivation of catalyst at particle-level in reactive flow is crucial to optimize the catalytic reactor.

5. Conclusions

A particle-resolved immersed boundary-lattice Boltzmann model is established to solve the bidirectional coupling between chemical reactions and particle dynamics: coke deposition alters motion through density changes, while particle trajectories modify reaction efficiency through flow-concentration interactions. The work explores how reaction rate constants k and initial release positions influence the hydrodynamic behavior of particles across five configurations: single particle, parallel/sequential particle pairs, cruciform clusters, and random arrangements.

Coke deposition increases particle density, disrupting force equilibrium and accelerating vertical settling velocity, particularly at higher k values. Catalyst particles exhibit significantly higher Re than inert particles, altering flow-field interactions. When k elevates Re beyond critical thresholds, vortex shedding induces abrupt motion changes during sedimentation. For two particles in parallel, increased k enhances horizontal oscillations, creating zigzag trajectories. While for the two particles in series, higher k accelerates DKT process until $k = 0.05$, under which condition the two particles would undergo the one-off DKT process. Multi-particle systems demonstrate suppressed average settling velocities due to amplified wall confinement effects, and slower sedimentation promotes greater coke accumulation compared to isolated particles. Particle motion dynamically redistributes reactant concentrations, creating heterogeneous catalyst deactivation process. Increased particle numbers and collisions further complicate coking rate dependencies.

This work enhances understanding the catalyst particles movement and transport process, providing insights for optimizing catalytic reactor designs. The model adopted in this work is a general model and can be extended to other reaction problems. Although the model successfully simulates the sedimentation of catalyst particles with coke deposition, the assumptions set for this learning model limit direct industrial applicability. In future, the influence of other factors, such as temperature, particle size and pore structure of catalysts will be introduced gradually to extend this method for more realistic catalytic reactions. Current limitations highlight the need to address simplified model assumptions in subsequent studies of practical catalytic systems.

CRediT authorship contribution statement

Yiqi Song: Writing – original draft, Validation, Software, Methodology, Investigation, Formal analysis, Conceptualization. **Xue Li:** Writing – review & editing, Supervision, Software, Investigation, Funding acquisition. **Mao Ye:** Writing – review & editing, Supervision, Resources, Project administration, Funding acquisition. **Zhongmin Liu:** Supervision.

Declaration of competing interest

The authors declare that they have no known competing financial interests or personal relationships that could have appeared to influence the work reported in this paper.

Acknowledgments

This work was financially supported by the National Natural Science Foundation of China (Grant Numbers: 22108269, 22293024, and 22293021), and the DICP Innovation Foundation (Grant Number: I202238) for supporting this work.

Data availability

The data that support the findings of this work are available from the corresponding author upon reasonable request.

References

Arcidiacono, S., Mantzaras, J., Karlin, I.V., 2008. Lattice Boltzmann simulation of catalytic reactions. Phys. Rev. E 78, 046711. https://doi.org/10.1103/PhysRevE.78.046711.

Behnam, M., Dixon, A.G., Nijemeisland, M., Stitt, E.H., 2010. Catalyst deactivation in 3D CFD resolved particle simulations of propane dehydrogenation. Ind. Eng. Chem. Res. 49, 10641–10650. https://doi.org/10.1021/ie100456k.

Eloul, S., Poon, W.C.K., Farago, O., Frenkel, D., 2020. Reactive momentum transfer contributes to the self-propulsion of janus particles. Phys. Rev. Lett. 124, 188001. https://doi.org/10.1103/PhysRevLett.124.188001.

Feng, Z., Michaelides, E.E., 2004. The immersed boundary-lattice Boltzmann method for solving fluid–particles interaction problems. J. Comput. Phys. 195, 602–628. https://doi.org/10.1016/j.jcp.2003.10.013.

Gan, H., Chang, J., Feng, J.J., Hu, H.H., 2003. Direct numerical simulation of the sedimentation of solid particles with thermal convection. J. Fluid Mech. 481, 385–411. https://doi.org/10.1017/S0022112003003938.

Ghosh, S., Kumar, M., 2020. Study of drafting, kissing and tumbling process of two particles with different sizes and densities using immersed boundary method in a confined medium. Appl. Math Comput. 386, 125411. https://doi.org/10.1016/j.amc.2020.125411.

Glowinski, R., Pan, T.W., Hesla, T.I., Joseph, D.D., Périaux, J., 2001. A fictitious domain approach to the direct numerical simulation of incompressible viscous flow past moving rigid bodies: application to particulate flow. J. Comput. Phys. 169, 363–426. https://doi.org/10.1006/jcph.2000.6542.

Gottifredi, J.C., Froment, G.F., 1997. A semi-analytical solution for concentration profiles inside a catalyst particle in the presence of coke formation. Chem. Eng. Sci. 52, 1883–1891. https://doi.org/10.1016/S0009-2509(97)00020-1.

Huang, R., Wu, H., 2014. A modified multiple-relaxation-time lattice Boltzmann model for convection–diffusion equation. J. Comput. Phys. 274, 50–63. https://doi.org/10.1016/j.jcp.2014.05.041.

Jafari, S., Yamamoto, R., Rahnama, M., 2011. Lattice-Boltzmann method combined with smoothed-profile method for particulate suspensions. Phys. Rev. E 83, 026702. https://doi.org/10.1103/PhysRevE.83.026702.

Kang, Q., Lichtner, P.C., Zhang, D., 2006. Lattice Boltzmann pore-scale model for multicomponent reactive transport in porous media. J. Geophys. Res. Solid Earth 111, B05203. https://doi.org/10.1029/2005JB003951.

Li, L., Mei, R., Klausner, J.F., 2017. Lattice Boltzmann models for the convection-diffusion equation: D2Q5 vs D2Q9. Int. J. Heat Mass Transf. 108, 41–62. https://doi.org/10.1016/j.ijheatmasstransfer.2016.11.092.

Li, X., Cai, J., Xin, F., Huai, X., Guo, J., 2013. Lattice Boltzmann simulation of endothermal catalytic reaction in catalyst porous media. Appl. Therm. Eng. 50, 1194–1200. https://doi.org/10.1016/j.applthermaleng.2012.08.058.

Lin, S., Zhi, Y., Liu, Z., Yuan, J., Liu, W., Zhang, W., Xu, Z., Zheng, A., Wei, Y., Liu, Z., 2022. Multiscale dynamical cross-talk in zeolite-catalyzed methanol and dimethyl ether conversions. Natl. Sci. Rev. 9, nwac151. https://doi.org/10.1093/nsr/nwac151.

Liu, J., Zhang, P., Xiao, Y., Wang, Z., Yuan, S., Tang, H., 2021. Interaction between dual spherical particles during settling in fluid. Phys. Fluids 33, 013312. https://doi.org/10.1063/5.0034927.

Liu, M., Shen, Z., Liang, Q., Liu, H., 2020. Particle fluctuating motions induced by gas-solid phase reaction. Chem. Eng. J. 388, 124348. https://doi.org/10.1016/j.cej.2020.124348.

Lu, J., Das, S., Peters, E.A.J.F., Kuipers, J.A.M., 2018. Direct numerical simulation of fluid flow and mass transfer in dense fluid-particle systems with surface reactions. Chem. Eng. Sci. 176, 1–18. https://doi.org/10.1016/j.ces.2017.10.018.

Luo, K., Mao, C., Fan, J., Zhuang, Z., Haugen, N.E.L., 2018. Fully resolved simulations of single char particle combustion using a ghost-cell immersed boundary method. AIChE J. 64, 2851–2863. https://doi.org/10.1002/aic.16136.

Maier, M.-L., Patel, R.A., Prasianakis, N.I., Churakov, S.V., Nirschl, H., Krause, M.J., 2021. Coupling of multiscale lattice Boltzmann discrete-element method for reactive particle fluid flows. Phys. Rev. E 103, 033306. https://doi.org/10.1103/PhysRevE.103.033306.

Molins, S., Soulaine, C., Prasianakis, N.I., Abbasi, A., Poncet, P., Ladd, A.J.C., Starchenko, V., Roman, S., Trebotich, D., Tchelepi, H.A., Steefel, C.I., 2021. Simulation of mineral dissolution at the pore scale with evolving fluid-solid interfaces: review of approaches and benchmark problem set. Comput. Geosci. 25, 1285–1318. https://doi.org/10.1007/s10596-019-09903-x.

Nie, D., Lin, J., 2020. Simulation of sedimentation of two spheres with different densities in a square tube. J. Fluid Mech. 896, A12. https://doi.org/10.1017/jfm.2020.291.

Nie, D., Lin, J., Gao, Q., 2017. Settling behavior of two particles with different densities in a vertical channel. Comput. Fluids 156, 353–367. https://doi.org/10.1016/j.compfluid.2017.07.021.

Niu, X.D., Shu, C., Chew, Y.T., Peng, Y., 2006. A momentum exchange-based immersed boundary-lattice Boltzmann method for simulating incompressible viscous flows. Phys. Lett. A 354, 173–182. https://doi.org/10.1016/j.physleta.2006.01.060.

Ou, Z., Guo, L., Chi, C., Zhao, J., Jin, H., Thévenin, D., 2022. Fully resolved direct numerical simulation of single coal particle gasification in supercritical water. Fuel 329, 125474. https://doi.org/10.1016/j.fuel.2022.125474.

Pu, D., Li, M., Shen, L., Wang, Z., Li, Z., 2023. The effects of channel width on particle sedimentation in fluids using a coupled lattice Boltzmann-discrete element model. Phys. Fluids 35, 053307. https://doi.org/10.1063/5.0147826.

Rahman Nezhad, J., Mirbozorgi, S.A., 2018. An immersed boundary-lattice Boltzmann method to simulate chaotic micromixers with baffles. Comput. Fluids 167, 206–214. https://doi.org/10.1016/j.compfluid.2018.02.031.

Sajjadi, H., Salmanzadeh, M., Ahmadi, G., Jafari, S., 2018. Investigation of particle deposition and dispersion using Hybrid LES/RANS model based on Lattice Boltzmann method. Sci. Iran. https://doi.org/10.24200/sci.2018.20723.

Sajjadi, H., Salmanzadeh, M., Ahmadi, G., Jafari, S., 2017. Lattice Boltzmann method and RANS approach for simulation of turbulent flows and particle transport and deposition. Particuology 30, 62–72. https://doi.org/10.1016/j.partic.2016.02.004.

Sajjadi, H., Salmanzadeh, M., Ahmadi, G., Jafari, S., 2016. Simulations of indoor airflow and particle dispersion and deposition by the lattice Boltzmann method using LES and RANS approaches. Build. Environ. 102, 1–12. https://doi.org/10.1016/j.buildenv.2016.03.006.

Shao, X., Liu, Y., Yu, Z., 2005. Interactions between two sedimenting particles with different sizes. Appl. Math. Mech. 26, 407–414. https://doi.org/10.1007/BF02440092.

Tian, P., Wei, Y., Ye, M., Liu, Z., 2015. Methanol to olefins (MTO): from fundamentals to commercialization. ACS Catal. 5, 1922–1938. https://doi.org/10.1021/acscatal.5b00007.

Krüger, T., Kusumaatmaja, H., Kuzmin, A., Shardt, O., Silva, G., Viggen, E.M., 2017. In: The Lattice Boltzmann Method: Principles and Practice, Graduate Texts in Physics. Springer International Publishing, Cham. https://doi.org/10.1007/978-3-319-44649-3.

Vogt, E.T.C., Weckhuysen, B.M., 2015. Fluid catalytic cracking: recent developments on the grand old lady of zeolite catalysis. Chem. Soc. Rev. 44, 7342–7370. https://doi.org/10.1039/C5CS00376H.

Wan, D., Turek, S., 2006. Direct numerical simulation of particulate flow via multigrid FEM techniques and the fictitious boundary method. Int. J. Numer. Methods Fluids 51, 531–566. https://doi.org/10.1002/fld.1129.

Wang, L., Guo, Z.L., Mi, J.C., 2014. Drafting, kissing and tumbling process of two particles with different sizes. Comput. Fluids 96, 20–34. https://doi.org/10.1016/j.compfluid.2014.03.005.

Wang, N., Zhi, Y., Wei, Y., Zhang, W., Liu, Z., Huang, J., Sun, T., Xu, S., Lin, S., He, Y., Zheng, A., Liu, Z., 2020. Molecular elucidating of an unusual growth mechanism for polycyclic aromatic hydrocarbons in confined space. Nat. Commun. 11, 1079. https://doi.org/10.1038/s41467-020-14493-9.

Wang, S., Qin, Z., Dong, M., Wang, J., Fan, W., 2022a. Recent progress on MTO reaction mechanisms and regulation of acid site distribution in the zeolite framework. Chem. Catal. 2, 1657–1685. https://doi.org/10.1016/j.checat.2022.05.012.

Wang, S., Yang, X., He, Y., 2022b. Pore-scale study of reactive transfer process involving coke deposition via lattice Boltzmann method. AIChE J. 68. https://doi.org/10.1002/aic.17478.

Wehinger, G.D., Eppinger, T., Kraume, M., 2015. Detailed numerical simulations of catalytic fixed-bed reactors: heterogeneous dry reforming of methane. Chem. Eng. Sci. 122, 197–209. https://doi.org/10.1016/j.ces.2014.09.007.

Yang, B., Chen, S., Cao, C., Liu, Z., Zheng, C., 2016. Lattice Boltzmann simulation of two cold particles settling in Newtonian fluid with thermal convection. Int. J. Heat Mass Transf. 93, 477–490. https://doi.org/10.1016/j.ijheatmasstransfer.2015.10.030.

Yang, L., Wang, C., Zhang, L., Dai, W., Chu, Y., Xu, J., Wu, G., Gao, M., Liu, W., Xu, Z., Wang, P., Guan, N., Dyballa, M., Ye, M., Deng, F., Fan, W., Li, L., 2021a. Stabilizing the framework of SAPO-34 zeolite toward long-term methanol-to-olefins conversion. Nat. Commun. 12, 4661. https://doi.org/10.1038/s41467-021-24403-2.

Yang, X., Wang, S., Zhang, K., He, Y., 2021b. Evaluation of coke deposition in catalyst particles using particle-resolved CFD model. Chem. Eng. Sci. 229, 116122. https://doi.org/10.1016/j.ces.2020.116122.

Yu, Z., Shao, X., Wachs, A., 2006. A fictitious domain method for particulate flows with heat transfer. J. Comput. Phys. 217, 424–452. https://doi.org/10.1016/j.jcp.2006.01.016.

Zavarukhin, S.G., Kuvshinov, G.G., 2004. The kinetic model of formation of nanofibrous carbon from CH4–H2 mixture over a high-loaded nickel catalyst with consideration for the catalyst deactivation. Appl. Catal. Gen. 272, 219–227. https://doi.org/10.1016/j.apcata.2004.05.044.

Zhang, M., Zhao, W., Lin, P., 2019. Lattice Boltzmann method for general convection-diffusion equations: MRT model and boundary schemes. J. Comput. Phys. 389, 147–163. https://doi.org/10.1016/j.jcp.2019.03.045.

Zhang, Y., Li, C., Ye, M., 2024. The role of permeability in lid-driven cavity flow containing a cluster of hot solids. Phys. Fluids 36, 043328. https://doi.org/10.1063/5.0200388.

Zhang, Y., Li, C., Ye, M., 2023. Motion of a two-dimensional neutrally buoyant circular particle in two-sided lid-driven cavity flow with thermal convection. Phys. Fluids 35, 123305. https://doi.org/10.1063/5.0169369.

Zhao, X., Hong, Y., Wang, L., Fan, D., Yan, N., Liu, X., Tian, P., Guo, X., Liu, Z., 2018. External surface modification of as-made ZSM-5 and their catalytic performance in the methanol to propylene reaction. Chin. J. Catal. 39, 1418–1426. https://doi.org/10.1016/S1872-2067(18)63117-1.

Zhao, Z., Xu, Z., 2022. Direct simulation on particle sedimentation mechanisms in corrosive liquids. Powder Technol. 404, 117503. https://doi.org/10.1016/j.powtec.2022.117503.

Zhou, J., Gao, M., Zhang, J., Liu, W., Zhang, T., Li, H., Xu, Z., Ye, M., Liu, Z., 2021. Directed transforming of coke to active intermediates in methanol-to-olefins catalyst to boost light olefins selectivity. Nat. Commun. 12, 17. https://doi.org/10.1038/s41467-020-20193-1.